Quantifying forcing uncertainties in the hydrodynamics of the Gironde estuary

Vanessya Laborie, Sophie Ricci, Matthias de Lozzo, Nicole Goutal, Yoann Audouin, Philippe Sergent

Computational Geosciences manuscript No.
(will be inserted by the editor)

Quantifying forcing uncertainties in the hydrodynamics of the Gironde estuary

Vanessya LABORIE · Sophie RICCI · Matthias DE LOZZO · Nicole GOUTAL · Yoann AUDOUIN · Philippe SERGENT

Received: 2018 07 07 / Accepted: date

Abstract High tide combined with high meteorological surge levels and discharges in the Garonne and Dordogne rivers in the Gironde estuary (south-west France), may lead to high water levels and flooding near the Blayais nuclear power plant and the city of Bordeaux, with significant economic and social impacts. A global sensitivity analysis (GSA) was performed with a Telemac2D numerical model currently used for operational water level forecasts. The major sources of uncertainties were identified by computing the Sobol' indices for uncertain inputs with an analysis of variance (ANOVA) approach for a 7-day storm event in 2003. The generation of the GSA ensemble of simulations consists of sampling scalar and field random variables: constant and uniform friction coefficients, as well as time-varying hydrological and maritime forcings. The temporal perturbation of time-dependent upstream hydrological and downstream maritime forcings is assumed to be represented by a Gaussian Process characterized by a correlation time scale calculated from observations. A Karhunen-Loève decomposition was then applied to retain a limited number of eigenmodes. The GSA is performed for 20 random variables using GENCI HPC computational resources for task parallelism and domain decomposition. This requires the use of 250 000 runs for an elapsed simulation time of 101 days on 32768 cores. The performance of the ensemble was assessed with a rank diagram and a reliability curve in comparison to a set of measured water levels at 12 observing stations along the estuary. It was shown that, for this event, the maritime boundary conditions and the Strickler coefficients have a predominant role along the length of the estuary with an influence driven by the tidal cycle. In the upstream fluvial areas, the friction coefficient and hydrological inputs are predominant.

Vanessya LABORIE
Saint-Venant Hydraulics laboratory, Cerema, 134, route de Beauvais, CS 60039, 60280 Margny Lès Compiègne, France
Tel.: +33-3-44416508
E-mail: vanessya.laborie@cerema.fr

Sophie RICCI
Ceci, Cerfacs/Cnrs, 42 avenue Gaspard Coriolis, 31057 Toulouse Cedex 01, France

Matthias DE LOZZO
Ceci, Cerfacs/Cnrs, 42 avenue Gaspard Coriolis, 31057 Toulouse Cedex 01, France

Nicole GOUTAL
Saint-Venant Hydraulics laboratory, Edf R&D, LNHE, 6 quai Watier, 78401 Chatou, France

Yoann AUDOUIN
Edf R&D, LNHE, 6 quai Watier, 78401 Chatou, France

Philippe SERGENT
Cerema, 134, route de Beauvais, CS 60039, 60280 Margny Lès Compiègne, France

Keywords uncertainty quantification · global sensitivity analysis · time-dependent forcings · Karhunen-Loève decomposition · Sobol' indices · Gironde estuary

Acknowledgements We would like to thank the service in charge of flood forecasting in the Garonne, Adour and Dordogne watersheds (SPC GAD), as well as METEO-FRANCE and the Great Maritime Port Councils of Bordeaux (GPMB) for the bathymetric and observational data they provided for this study. The sea level observations along the Gironde estuary are the property of GPMB and the French Ministry in charge of sustainable development (MTES). This work was granted access to the HPC resources of IDRIS under the allocation 2017-A0030110292. The authors sincerely thank Sylvie THEROND and Isabelle DUPAYS at IDRIS, for technical support, as well as Marissa YATES-MICHELIN for helping out with the proofreading of this article.

1 Introduction

Environmental, economical and security issues are at stake in the Gironde estuary catchment located in South-West France near the city of Bordeaux and the nuclear power plant of Blayais. The Dordogne and Garonne rivers meet at Bec d'Ambès and the estuary reaches the Atlantic Ocean coastline about 75 km further downstream. The estuary is subject to maritime influences and the combination of strong tidal amplitudes with high fluvial inflows can lead to strong flood events [1]. Governmental agencies are responsible for the safety of people and property. They rely on Decision Support Systems to take preventive measures to alert communities and to coordinate crisis management. Since the most severe flood event on record in the Gironde estuary in 1770, infrastructures were built to limit the consequences of flooding, yet these failed to protect fully the area during strong events such as Lothar and Martin in 1999 and Xynthia in 2010. The overflowing of dikes protecting the Blayais nuclear power plant in 1999 demonstrated the strong need for water level forecasts in the estuary. In France, the SCHAPI (Service Central d'Hydrométéorologie et d'Appui à la Prévision des Inondations) and Flood Forecast Services (FFS) are in charge of monitoring and forecasting water levels and discharge over 22 000 km of rivers. They produce a twice-daily vigilance colored-risk map available online for governmental authorities and the general public (http://www.vigicrues.gouv.fr). To create these risk maps, they rely on numerical models and in-situ measurements [2].

Hydrodynamic numerical software packages based on the Shallow-Water Equations (SWE) are commonly used tools to aid in the management and protection of urban infrastructures located near rivers and coasts. They are also used for operational flood forecasting. Yet, these numerical codes remain imperfect as uncertainties in the models and in the inputs (model parameters, boundary conditions, geometry, etc.) propagate into uncertainties in the outputs (water levels, discharge). Quantifying physical uncertainties goes beyond the limits of deterministic forecasting and represents a significant challenge. The FFS Garonne-Adour-Dordogne (GAD) is in charge of the Gironde estuary area. In order to meet operational expectations, especially for extreme events, FFS GAD moved from a statistical model based on climatological data to a numerical model that solves the SWE based on the hydraulic software Telemac2D [3]. The Gironde estuary model was limited to the non-overflowing area, excluding the floodplains owing to computational constraints in an operational context. Despite this limitation, it resulted in improving water level forecast skill and increasing alert lead-times. While this model provides good results for past events in reanalysis mode, with errors of less than 10 cm for non-overflowing scenarios, simulating high tides periods is more challenging and in overflowing situations, errors of the order of 30 cm remain near Bordeaux. The 'Gironde project' [4] recommended areas for improvement including updating the model state and parameters with data assimilation algorithms. To do so, the major sources of uncertainty amongst the numerous uncertain numerical data, input data and forcing data should be identified, quantified and reduced.

This paper presents a Sensitivity Analysis (SA) study in the context of flood forecasting in the Gironde estuary. It aims at identifying and classifying the major sources of uncertainties that limit the predictive capability of water levels and discharge from the fluvial upstream boundaries to the downstream Atlantic coastline, focusing on locations of interest where safety and economical assets are at stake [5].

A wide range of SA methods are proposed in the literature [6] to estimate the contribution of uncertain model parameters and inputs to the uncertainty in the model Quantities of Interest (QoI). On the one hand, local SA approaches provide the sensitivity of the model outputs with respect to the model inputs around a reference value using the tangent linear of the model (when available) or finite differences techniques. On the other hand, Global SA approaches (GSA) provide the contribution to the QoI's uncertainty from the uncertain input parameter when varying over the whole input parameter space. The ANOVA (ANalysis Of VAriance) method consists in estimating the QoI variance decomposition in terms of elementary variances associated with the different parameters and their interactions [7]. This decomposition is obtained from a Proper Orthogonal Decomposition of the uncertain QoI over the probabilized parameter space [8]. Sensitivity indices, called Sobol' indices, represent the contribution of each parameter and their interactions to the model output variance. The ANOVA approach is suited even for non linear and non monotonic models ([9], [10]) provided that the uncertain parameters are uncorrelated and independent [11].

GSA requires the integration of a large number of simulations with a direct model. In spite of increasing High Performance Computing (HPC) resources, the ensemble's computational cost is still incompatible with operational or industrial applications. Monte Carlo random sampling techniques are often used as they are generic, robust, and easily portable on massively parallel architectures. Yet, they remain computationally expensive due to their slow convergence rate, which scales

as the inverse of the square root of the number of members [12]. Using a Sobol' sequence space-filling strategy is prefered to compute first and total Sobol' sensitivity indices [10] and to assess the contribution of each uncertain variable and their interactions to the total variability of the system. When uncertainties are associated with field inputs, for instance discretized over time and/or space, the cost of Monte Carlo-based GSA becomes untrackable and advanced solutions should be adopted. One approach consists in replacing the direct solver with a meta (or surrogate) model built from a limited number of integrations of the direct solver ([13], [14], [15], [16], [17]). The quality of the surrogate depends on the complexity of the physics, for instance the non-linearity between inputs and outputs of the model, the size of the learning sample, and the surrogate strategy. Various metamodeling algorithms are proposed in the literature. [18] gives an overview of metamodeling approaches adapted to uncertainty propagation and GSA. This approach is beyond the scope of the present study. When the dimension of the uncertain space is large, the GSA is carried out in a reduced space with a Proper Orthogonal Decomposition [19]. The Proper Orthogonal Decomposition (also refereed to as Principal Component Analysis or Karhunen-Loève (KL) decomposition) is a procedure for extracting a basis of a modal decomposition from an ensemble of signals [20]. Its power lies in the mathematical properties that suggest that it is the appropriate basis, as it is a linear procedure and makes no assumptions on the linearity of the problem to which it applies. The KL decomposition minimizes in the mean squared sense the representation error.

GSA is often used to classify the sources of uncertainties for large scale hydrology as well as for hydrodynamics at the scale of French rivers, assuming the uncertainties originate from scalar inputs. A multivariate GSA based on the ANOVA technique was applied in the Amazon River basin by [21] to highlight the major sources of errors in the river water level and discharge simulated by the river-routing scheme Total Runoff Integrating Pathways (TRIP). By assuming a particular input uncertainty distribution, it was shown that geomorphological parameters explain most of the water level variance with purely additive contributions from the river Manning coefficients, riverbed slope and river width. [22] presented a Sobol' SA for flow simulation by a SWAT (Soil And Water Assessment Tool) model of river, for a complex environmental system controlled by a large number of parameters (about 30). It was shown that even with a limited number of direct solver evaluations, the GSA identified the most significant parameters and improved the understanding of the model behavior. [23] presents an overview of SA studies for the Garonne river in steady flow conditions with both local SA and GSA. The details for the local SA are given in [24]. The 1.5D hydraulic model SIC (Irstea) is used within a variational framework implying its tangent linear and adjoint codes to acknowledge the impact of the geometry, friction coefficient and upstream discharge on the water level and discharge discretized along the 50-km river reach. The GSA was carried out with both 1D and 2D solvers Mascaret-Telemac (Electricité de France) with a Monte Carlo approach as well as with a polynomial surrogate model. When uncertainties stem from field data, such as meteorological (wind, pressure, temperature) fields or river discharges for example, the cost of Monte Carlo-based GSA drastically increases, and the computation of the surrogate becomes challenging. [25] presents solutions to perform GSA with field inputs and outputs to the numerical code NOE which is a spatial model for cost-benefit analysis of flood risk management plans and which is used to assess, through simplified equations, the economic impact of flood risk [26]. [27] uses empirical orthogonal functions and analyzes the combined impact of uncertainties in initial conditions and wind forcing fields in ocean general circulation models using polynomial chaos (PC) expansions.

In the context of the Gironde estuary study, the uncertainties depend on the time-varying hydrological upstream forcing and on maritime boundary conditions, the space and time-varying bathymetry, and wind and pressure forcing, the space-varying bottom friction coefficients (4 scalars defined by uniform areas), and the wind drag coefficient (scalar). Only uncertainties that relate to friction and wind drag coefficients, hydrological and maritime forcing are taken into account here. The SA with respect to surface forcing is beyond the scope of the present study. A KL expansion is used to reduce the size of the time-dependent uncertain inputs, assuming that each perturbation of the observed forcing is a gaussian process characterized by a correlation function and a correlation time scale. The originality of the present study is that a GSA is performed on unsteady flows simulations using the Telemac2D solver, while accounting for the maritime influence of the Gironde estuary. Beyond the central objective of the GSA, the scope of the study is to build a reference case which will enable future work with data assimilation techniques, but also on metamodels or multi-fidelity simulations applied to the Gironde estuary site. Moreover, the hydrodynamics of the Gironde estuary results from varying power balancing between the space- and/or time-dependent friction, geometry and both upstream and downstream boundary conditions, which complicate the

immediate and intuitive interpretation of the complex hydrodynamics of the estuary. Quantifying uncertainties both in space and time, and identifying the most influential variables can thus help to understand the dominant physical processes in the estuary.
The structure of the paper is as follows. Section 2 presents the materials and methods for the GSA. Section 2.1 presents the Gironde estuary, SWE and the hydrodynamic model implemented with Telemac2D. Section 2.2 describes the computation of sensitivity indices. The ensemble generation and sensitivity analysis with field inputs techniques are described in Sect. 2.3. Details on the HPC resources and performance of the ensemble are also detailed. Statistics drawn from the ensemble are presented in Sect. 3: the water level probability density function is shown at specific locations along the estuary and the Sobol' indices are plotted as a function of time and space. The focuses on the sensitivity to the maritime boundary forcing eigenmodes, conclusions and perspectives for the study are finally presented.

2 Framework

2.1 Hydrodynamic model of the Gironde estuary

2.1.1 Presentation of the Gironde estuary

The Gironde estuary is the largest macrotidal estuary in France and Western Europe. The Gironde estuary extends from the Bay of Biscay approximately 170 km inland and covers a surface of 635 km^2. It is located in southwest France. Created from the confluence of two rivers (Garonne and Dordogne rivers), it extends 75 km to reach the mouth of the estuary at the Atlantic coastline (Fig. 1). On average, it is oriented from south-east to north-west in a valley, and its width ranges from 1 km near Bordeaux to 15 km at the coast. The Gironde estuary can be divided [28] into three subdomains: the upstream river area, the central estuary area and the downstream offshore area [29]. The estuary can be classified as macrotidal, hypersynchronous, and with an asymmetric tide (4 h for the flood and 8 h 25 min for the ebb). The tide in the Bay of Biscay is semidiurnal, with a period of 12 h 25 min and is dominated by the principal semidiurnal lunar (M2) component. The open ocean induces a strong tidal forcing with a tidal amplitude near the mouth of the estuary ranging from 2.2 to 5.4 m over the spring-neap cycle. The Garonne (resp. Dordogne) river discharge typically ranges from 50 (resp. 20) up to 2 000 (resp. 1 000) m^3.s^{-1}. During flood events, the Garonne flow rate occasionally exceeds 5 000 m^3.s^{-1}. The economic importance of the Gironde estuary is evidenced by the presence of large cities and ports, including the city of Bordeaux and the Harbor of Bordeaux, as well as by the presence of various industries, such as the Blayais nuclear power plant, fisheries and tourism activities. The flooding risk has been a major concern for authorities along the Gironde estuary [1] for a long time, as shown by historical documents dating from the XIII$^{\text{th}}$ century. The most damaging flood occurred in April 1770, when about 24 000 km^2 were covered by water along the Garonne river and the Gironde estuary, causing about 4,669 million euros in damage exclusively in the city of Bordeaux (35 million euros using purchasing power parity for primary goods). From this point, flood protection structures were built to limit the consequences of flooding. However, this did not prevent strong floods in 1835, 1855 and 1856. In 1930, floods caused the destruction of 1 000 houses and more than 300 casualties. In recent decades, three notable events were observed: the December 1981 event, which was caused by strong river discharges during high tides, and the Lothar and Martin storms in 1999 and Xynthia in 2010 [30].

2.1.2 Shallow water equations in Telemac2D

The SWE are commonly used in environmental hydrodynamics modelling. They are derived from the Navier-Stokes equations and express mass and momentum conservation averaged in the vertical dimension. The non-conservative form of the equations are written in terms of the water depth (h [m]) and the horizontal components of velocity (u and v [m.s^{-1}]).

$$\frac{\partial h}{\partial t} + \frac{\partial}{\partial x}(hu) + \frac{\partial}{\partial y}(hv) = 0 \tag{1}$$

$$\frac{\partial u}{\partial t} + u\frac{\partial u}{\partial x} + v\frac{\partial u}{\partial y} = -g\frac{\partial H}{\partial x} + F_x + \frac{1}{h}div\left(h\nu_e\overrightarrow{grad}(u)\right) \tag{2}$$

$$\frac{\partial v}{\partial t} + u\frac{\partial v}{\partial x} + v\frac{\partial v}{\partial y} = -g\frac{\partial H}{\partial y} + F_y + \frac{1}{h}div\left(h\nu_e\overrightarrow{grad}(v)\right) \tag{3}$$

where:

$$\begin{aligned} F_x = &- \frac{g}{{K_s}^2}\frac{u\sqrt{u^2+v^2}}{h^{\frac{4}{3}}} - \frac{1}{\rho_w}\frac{\partial P_{atm}}{\partial x} \\ &+ \frac{1}{h}\frac{\rho_{air}}{\rho_w}\ C_d\ U_{w,x}\sqrt{U_{w,x}^2+U_{w,y}^2} \end{aligned} \tag{4}$$

$$F_y = -\frac{g}{{K_s}^2}\frac{v\sqrt{u^2+v^2}}{h^{\frac{4}{3}}} - \frac{1}{\rho_w}\frac{\partial P_{atm}}{\partial y} + \frac{1}{h}\frac{\rho_{air}}{\rho_w}\ C_d\ U_{w,y}\sqrt{U_{w,x}^2+U_{w,y}^2} \quad (5)$$

and ρ_{air}/ρ_w [kg.m^{-3}] are the air/water density, P_{atm} [Pa] is the atmospheric pressure, $U_{w,x}$ and $U_{w,y}$ [m.s^{-1}] are the horizontal wind velocity components, C_d [-] is the wind drag coefficient that relates the free surface wind to the shear stress, K_s [m$^{\frac{1}{3}}$.s^{-1}] is the river bed and floodplain friction coefficient, using the Strickler formulation [31]. F_x and F_y [m.s^{-2}] are the horizontal components of external forces (friction, wind and atmospheric forces), H [m NGF69] is the water level ($h = H - z_f$ if z_f [m NGF69] is the bottom level) and ν_e [m^2.s^{-1}] is the water diffusion coefficient. *div* and $\overrightarrow{grad}$ are respectively the divergence and gradient operators. To solve the system of equations Eq. (1) to Eq. (3), initial conditions $h(x,y,t=0) = h_0(x,y)$; $u(x,y,t=0) = u_0(x,y)$; $v(x,y,t=0) = v_0(x,y)$ are provided. Boundary conditions (BC) both at the coastline (slip and impermeability conditions) and at the upstream and downstream boundaries ($h(x_{BC}, y_{BC}, t) = h_{BC}(t)$) are also given.
In the present study, the SWE are solved with the parallel numerical solver Telemac2D (www.opentelemac.org) with an explicit first-order time integration scheme, a finite element scheme and an iterative conjugate gradient method [3]. In the following, we will take into account parametric uncertainties, that are due to the stochastic nature of the atmosphere-surface system. These include the forcing fields and epistemic uncertainties that come from a lack of knowledge concerning the physical processes of the hydrodynamic system, leading to a simplified parametrization, such as friction or turbulence, but also the imperfect description of the system, such as the geometry of the river. These uncertainties can be represented by independent scalars (friction coefficients) or time and/or space correlated discretized fields (fluvial, atmospheric and maritime forcings).

2.1.3 The Gironde estuary numerical model

A hydrodynamic numerical model of the Gironde estuary (Fig. 1), based on Telemac2D and on a bathymetry / topography field (Fig. 2), is used operationally to compute the water depth and velocity in the estuary and along the Garonne and Dordogne rivers. The maritime boundary is located in the Gascogne Gulf, 35 km away from le Verdon. The upstream boundaries are located at La Réole on the Garonne River and at Pessac on the Dordogne River. It should be noted that inflows from the Isle and Dronne rivers are artificially injected at Pessac [4] and that floodplains are not taken into account. The operational numerical model used by FFS GAD covers about 125 km from east to west, features 12838 finite elements and is composed of 7351 nodes (coarse mesh). Refined meshes (27546 nodes, 106450 nodes and 418314 nodes) were built for a convergence study. It was shown that mesh convergence is obtained for water levels (using a 5 cm error threshold) in the entire estuary except in the fluvial areas for meshes with more than 106450 nodes. The 418314 node fine mesh was thus used in the following for SA. Hydrological upstream forcings for the Dordogne and Garonne rivers are provided by the DREAL (Direction Régionale de l'Environnement, de l'Aménagement des Territoires et du Logement) Nouvelle Aquitaine at a 1-hour time step. Surface wind velocity and pressure fields from the regional meteorological model ALADIN [32] are provided by Meteo-France at a 3-hour time step. Water levels at the maritime boundary are the sum of the predicted astronomical tide and surge levels; these data are also provided in real-time by Meteo-France every 10 to 15 min. The friction coefficient is uniformly defined over 4 areas as shown in Fig. 1. The model calibration was achieved during the non-flooding 2003 event to optimize either the water level Root Mean Square Error (*RMSE*, Eq. (6)) or the Nash criteria at high tide ($Nash_{HT}$, Eq. (7)) computed between simulated and observed water levels available at the 12 stations among the 26 stations of interest shown with red stars in Fig. 2. Two sets of friction coefficients were obtained from the calibration and are presented in Table 1. The resulting *RMSE* and $Nash_{HT}$ scores for the 2003 event are presented in Table 2 along with the evaluation scores for the 1999 flooding event. The $Nash_{HT}$ (Eq. (7)) is evaluated at high tide and the *RMSE* (Eq. (6)) (resp. $RMSE_{HT}$) is evaluated by summing over the entire flood event (resp. at high tide):

$$RMSE = \sqrt{\frac{1}{n}\sum_{i=1}^{n}(H_i - \widehat{H_i})^2} \quad (6)$$

$$Nash_{HT} = 1 - \frac{\sum_{i=1}^{n}(H_i - \widehat{H_i})^2}{\sum_{i=1}^{n}(\widehat{H_i} - \overline{H})^2}, \quad (7)$$

where n is the time index, H_i and $\widehat{H_i}$ are the simulated and observed water levels and $\overline{H}$ the time-averaged observed water levels. As expected, the *RMSE* and $Nash_{HT}$ scores are significantly better for the 2003 non-flooding calibration event than for the 1999 flooding evaluation event. The water level *RMSE* reaches 16 cm at Le Verdon and 36 cm at Laména in 2003 and 2.0 m

at Le Verdon and 1.49 m at Laména for the overflowing event in 1999. These errors remain higher than the target 10 cm precision expected by FFS GAD. These results are computed over past events in reanalysis mode using perfect meteorological and hydrological forcing. Additional errors due to imperfect forecasting are expected in operational mode, especially with increasing lead time [4]. The scores obtained for calibration and evaluation events, especially in flooding conditions, advocate further improvement of the Gironde model with the assimilation of observed water levels.

The wind drag coefficient formulates the wind shear stress at the free surface from the wind velocity [33]. A uniform and constant value was chosen here ($C_d = 2.14\ 10^{-3}$) consistently with the calibration of the surge level numerical model for the Atlantic Ocean, English Channel and North Sea [34].

2.2 Computation of sensitivity indices

2.2.1 Variance decomposition and Sobol' indices

Sobol' indices [35] measure the contributions of the different independent inputs $X_1, X_2, \ldots, X_d$ and their interactions in the variance V(Y) of the output $Y = f(X)$ with $X = (X_1, X_2, \ldots, X_d)$, $E((f(X))^2) < \infty$ and f the model. $S_i = \frac{V_i}{V(Y)}$ is the first-order Sobol' index of X_i, representing the normalized elementary contribution of X_i to $V(Y)$. $S_{i,j} = \frac{V_{i,j}}{V(Y)}$ is the second-order Sobol' index of X_i and X_j, representing the normalized contribution of the interaction between X_i and X_j to $V(Y)$, and so on. As described in Appendix A, using Eq. (8):

$$1 = \sum_{i \subseteq I_d} S_i + \sum_{\substack{\{i,j\} \subseteq I_d^2 \\ j>i}} S_{i,j} + \ldots + S_{1,2,\ldots,d} = \sum_{u \subseteq I_d} S_u \quad (8)$$

where: $I_d = \{1, \ldots, d\}$ is the set of input indices, the total Sobol' index S_{T_i} gathering all contributions related to X_i is then defined as:

$$S_{Ti} = S_i + \sum_{\substack{j \in I_d \\ j>i}} S_{i,j} + \ldots + S_{1,2,\ldots,d} = \sum_{\substack{u \subseteq I_d \\ u \ni i}} S_u \quad (9)$$

It should be noted that $\sum_i S_i = 1$ if there is no interaction between the input parameters.

2.2.2 Implementation of Sobol' indices computation

The main steps for the stochastic estimation of the Sobol' indices of the different independent inputs $X_1, X_2, \ldots, X_d$ with $X = (X_1, X_2, \ldots, X_d)$ are described in Appendix B according to [10], which the reader can refer to for more details.

It should be noted that the calculation of the first and total Sobol' indices for an ensemble of size N requires the integration of two independent samples. Given d uncertain variables and N_e perturbed members for each variable, the total number of simulations is thus $N = N_e(d+2)$.

If $(X_i)_{i=k,,k+m}$ correspond to the m uncertain modes of a field input, the contribution of each mode can be estimated separately with the methodology described in Appendix B, but also the whole contribution of the field input. If k_m denotes the number of uncertain field variables whose contribution is estimated in addition to the contribution of each mode, then the total number of simulations is $N = N_e(d+2+k_m)$.

2.3 Ensemble generation with field inputs

2.3.1 Uncertain space for SA in the Gironde estuary

The GSA study was carried for the 7-day February 2003 event with a tide coefficient in the range [43 ; 90], Dordogne upstream discharge (resp. Garonne) in the range [600 ; 2200] $m^3.s^{-1}$ (resp. [1200 ; 5900] $m^3.s^{-1}$).

The present study has $d = 8$ uncertain sources: the 4 zone-distributed scalar friction coefficients (Ks1, Ks2, Ks3, Ks4), the scalar wind drag coefficient Cd, and the time-dependent boundary conditions at the hydrological limits (QDOR and QGAR for the Dordogne and Garonne rivers respectively) and at the maritime limit (CLMAR). Additional sources of uncertainty, such as space- and time-varying meteorological forcing or bathymetry, exist and have not been considered in the study. The uncertain input vector is denoted by $X = (X_i)_{i \in I_8}$ where X_1 = Ks1, X_2 = Ks2, X_3 = Ks3, X_4 = Ks4, X_5 = Cd, X_6 = QDOR, X_7 = QGAR and X_8 = CLMAR. The QoI is the water level defined over the simulation domain at a given time, with 26 stations that are of particular interest (see Fig. 2). The water level at a given location is a scalar denoted by Y in the following.

The wind drag coefficient and friction coefficients are supposed to follow uniform distributions with ranges described in Table 1. [33] presents a review of parametric formulations of the wind drag coefficient based on [36], [37], [38]. These parametric formulations were used for the Gironde case using climatological wind intensities (Climate Forecast System Reanalysis from NOAA) to define the range for the Cd uniform distribution. The ranges of the friction coefficients are chosen so as to include the calibration values for the 2003 event using both the $Nash_{HT}$ and $RMSE$ criteria. The interval

corresponds to the commonly accepted uncertainty on friction for engineering studies.

The time-dependent hydrological forcing is assumed to be perturbed by an additive centered Gaussian process $q(t)$. The covariance of $q(t)$ is defined by a squared exponential kernel $\kappa(t,t') = \sigma^2 \exp(-\ell^{-2}(t-t')^2)$, where ℓ is the correlation time scale estimated from observations over the 1981-2016 period, and the standard deviation σ is the amplitude of the perturbation. The time dependent maritime forcing is also assumed to be perturbed by an additive Gaussian Process $h(t)$ with a gaussian covariance function. A truncated form $q_p(t)$ (resp. $h_p(t)$) of $q(t)$ (resp. $h(t)$) is formulated with a KL decomposition [20] of $q(t)$ (resp. $h(t)$).

Numerically, as explained in Appendix C, the eigenfunction problem defined by the Fredholm equation is approximated by the eigenvector problem defined over the discretized time series $\{t_1, t_2, \ldots, t_N\}$:

$$K\Phi_i = \lambda_i \Phi_i \tag{10}$$

where $\Phi_i = (\phi_i(t_1) \ldots \phi_i(t_N))^T$, $K = (\kappa(t_i,t_j))_{1\leq i,j\leq p}$ and (λ_i, ϕ_i) are the i^{th} eigenvalue and eigenfunction of κ, the solution of the Fredholm equation [39].
The solution (λ_i, Φ_i) of Eq. (10) is obtained from a singular value decomposition (SVD) and contributes to the truncated expansion of $q(t)$ (and $h(t)$) discretized over the discretized time series:

$$q_p = (q_p(t_1), \ldots, q_p(t_N))^T = \sum_{i=1}^{p} \sqrt{\lambda_i} \Phi_i \epsilon_i. \tag{11}$$

where ϵ_i are independent standard Gaussian variables. Last but not least, based on the property $\sum_{i=1}^{p} \lambda_i = \sigma^2$, the degree of truncation p is chosen such that the fraction of the total variance $\sum_{i=1}^{p} \lambda_i \sigma^{-2}$ exceeds a threshold the closest to one.

Sampling the perturbation $q(t)$ (resp. $h(t)$) associated with the time-dependent hydrological (resp. maritime) forcing over the discretized time series $\{t_1, t_2, \ldots, t_N\}$ sums up sampling the random vector q_p (resp. h_p), as sampling p independent standard Gaussian variables. Fig. 3-a and Fig. 3-b present a set of 7 perturbations of the boundary condition $q(t)$ at the Garonne upstream location and $h(t)$ at the maritime boundary.

The boundary condition resulting from the aforementioned perturbed signal is displayed in Fig. 3-c for the Garonne and in Fig. 3-d for the maritime boundary. The autocorrelation time scale was estimated for about 10 discharge signals during major flood events on the Garonne and Dordogne rivers. The correlation time scales ℓ_{QGAR} and ℓ_{QDOR} are thus set to 3 days for the 2003 event and the correlation time scale ℓ_{CLMAR} is set to 6 hours (approximately half a tidal cycle) for the maritime boundary. The amplitudes σ_{QDOR} and σ_{QGAR} of the perturbations of the upstream discharges are set proportional (20 %) to the observed discharges as the uncertainties of the rating curves used to translate the water levels into discharges are larger for high flow time series. The amplitude σ_{CLMAR} of the maritime boundary condition perturbation is set to 50 cm, representing the sum of the uncertainties in surge levels and in the predicted offshore tide, at the maritime boundary of the numerical model. The KL decompositions of the hydrological and maritime forcings are respectively truncated to $p_{\text{QDOR}} = p_{\text{QGAR}} = 4$ and $p_{\text{CLMAR}} = 7$ modes, retaining respectively 90 % and 45 % of the Gaussian process variability. This value, associated to ℓ_{CLMAR}, will be discussed in Sect. 3.4. Moreover, the KL modes will be either aggregated or treated separately in the following for Sobol' indices formulation. The GSA is thus carried out in an uncertain space described by 20 variables: Ks1, Ks2, Ks3, Ks4, Cd, 4 modes for each hydrological boundary condition (QGAR and QDOR) and 7 modes for the maritime boundary condition CLMAR.

2.3.2 High Performance Computing resources

The GSA for the 2003 event was performed using both coarse and fine meshes. Due to computational constraints, it was only carried out over one tidal cycle with the fine mesh. Yet the conclusions drawn for the GSA over this period with the fine mesh are similar to those drawn for the coarse mesh over the 7-day event. As a consequence, in the following, illustrations for the GSA are given for the coarse mesh model. Computational resources for the GSA are given in Table 3. For the fine mesh, the convergence of the GSA results was investigated with increasing number of members N_e ranging from 100 to 10000. The Sobol' indices reach convergence for all variables over the simulation time period (not shown) from $N_e = 2000$. The simulations were performed on the HPC resources from GENCI-IDRIS (grant 2017-A0030110292).
For coarse and fine meshes (Table 3 - Col. 1), the simulated period is indicated in Table 3 - Col. 2. For each HPC architecture (Table 3 - Col. 9), a scalability study was performed for a single run with domain decomposition: the optimal number of cores is shown in Table 3 - Col. 3 along with the elapsed time in Table 3 -Col. 4. The GSA involves both domain decomposition and task parallelism. The total number of available cores for the GSA is shown in Table 3 - Col. 5. As Sobol' indices are computed for field inputs considering the contribution of each mode only and also the whole contribution of the uncertain variable, the ensemble size N_e and the

total number of simulations N are given in Table 3 - Col. 6 and Col. 7 respectively. Finally, the elapsed time for the GSA is given in Table 3 - Col. 8.

3 GSA results

The GSA study was carried for the 7-day February 2003 event with a tide coefficient in the range [43 ; 90], Dordogne (resp. Garonne) upstream discharge in the range of [600 ; 2200] $m^3.s^{-1}$ (resp. [1200 ; 5900] $m^3.s^{-1}$).

3.1 Performance of the ensemble

3.1.1 Description of the criteria

The performance of the ensemble forecasts is commonly assessed with criteria such as consistency and reliability [40]. The former measures the average spread of an ensemble compared to observations, whereas the latter generally reflects the accuracy of a forecast model.
The consistency criterion characterizes the coherence between the distribution of the ensemble members and a set of observations through the use of the rank histogram [41] for a given simulation time or over a simulation period. The ensemble values are ranked in classes, and the occurrence of the observed value within these classes is computed and represented with a rank histogram. Fig. 4 displays the rank histogram at stations Le Verdon, Richard and Bec d'Ambès for all time steps during the 2003 event. It is expected to be flat when the ensemble members and the observations follow similar distributions, U-shaped when the ensemble is under-dispersive, and bump-shaped when the ensemble is over-dispersive. Here, the occurrence is normalized by the ensemble size and is displayed in Fig. 5 with a blue-red color bar along the curvilinear abscissa (x-axis) of 12 observing stations as a function of time (y-axis). This time and space distributed representation allows the determination of when and where the ensemble is consistent with the observations (ranks uniformly distributed from 0.1 to 0.9) or not (extreme rank values equal to 0 when the ensemble over estimates water levels, and rank values equal to 1 when the ensemble under estimates water levels).
The reliability criterion evaluates the coherence between the forecasted and the observed probabilities of an event [42]. An event is defined as $Z >= Z_T$, where Z is the random value simulated in the ensemble and Z_T is the threshold value. The reliability plot represents the observation probability for the events with respect to the simulated probability. The ensemble is reliable if the relation follows the first bisector line; it is under or over dispersive otherwise. The reliability criterion for 4 observing stations (Le Verdon, Richard, Bec d'Ambès and La Réole) is represented in Fig. 6. Over each curve, the observation quantiles (q_{10} to q_{90}) are represented with circles (q_{50} represented by a larger symbol). Reliability curves under (resp. above) the perfect reliability diagonal curve reveal an over-predictive (resp. under-predictive) ensemble.

3.1.2 Interpretation of water level ensemble performance

Considering both performance criteria in Fig. 4, Fig. 5 and Fig. 6, it appears that the performance of the ensemble is closely related to the tidal cycle and the location in the estuary. At Le Verdon (resp. Richard), at the mouth of the estuary, the reliability curve (blue (resp. green) curve) shows that the ensemble is slightly under- (resp. over-) predictive for all quantiles with water levels that are under- (resp. over-) estimated. Considering the corresponding locations of Fig. 5 for each of them shows respectively a predominance of red and blue nuances independent of the tidal cycle. For water levels lower than the mean tide water level, this can be explained at Le Verdon by a truncated observed signal during the 2003 event. Moreover, calibration results (Table 2) have shown the trend of the numerical model to under-estimate water levels at Le Verdon and to over-estimate them at Richard during flood tide, as the mean error for high tides are respectively negative (-12 cm at Le Verdon) and positive (+21 cm at Richard). In the middle part of the estuary, from Laména to Bordeaux, Fig. 4 shows a tide-dependent rank. The ensemble is over-predictive at low tide and under-predictive at high tide, as suggested in Fig. 6 by the reliability curve at Bec d'Ambès (red line). The Bec d'Ambès reliability curve is under the perfect diagonal reliability curve for water quantiles lower than the mean tide level and above this curve for quantiles higher than the mean tide level. This reflects calibration choices for a better representation of high tides leading to under-dispersive behavior. Indeed, the reliability curve exhibits smaller distances to the diagonal for higher water levels than for lower ones. At the upstream part of Garonne and Dordogne rivers, Fig. 4, Fig. 5 and Fig. 6 show a strong under-predictive signature of the ensemble at La Réole and an over-predictive signature at Pessac (for the end of the storm). This highlights the need for a more refined mesh in the fluvial part of the model.
The ensemble performance has been assessed. It shows that the over/under predictive signature or non-reliability is directly linked to the numerical model calibration or to the mesh refinement in the fluvial areas.

3.2 Water level probability density function

The water level mean and standard deviation are displayed with a blue-red color bar along the curvilinear abscissa (x-axis) of the 26 stations of interest as a function of time (y-axis) in Fig. 7. Fig. 7-a shows the ensemble mean water level; it illustrates the propagation of tides from the mouth of the estuary to the upstream part of the Garonne and Dordogne rivers. The hypersynchronic characteristic of the Gironde estuary due to a funnel effect leads to the amplification of high tides in the estuary from the decreasing water depth in bathymetry. The absolute differences of the median with 95%-quantile and 5%-quantile (not shown) shows a nearly perfect symmetry of the distribution of QoIs between its extreme quantiles. The standard deviation plotted in Fig. 7-b increases from 20 cm at Royan to 45 cm at Pessac and La Réole for high tides.
Fig. 8 displays the PDF of water level anomalies (with respect to the ensemble mean) at the storm peak (a), ebb tide (b), low tide (c) and flood tide (d) for 14 observing stations (blue curves for the maritime boundary, green for the estuary, yellow, orange and red for the Garonne and Dordogne rivers). Upstream of the fluvial areas, the PDF is asymmetric for all times with a median value of about -40 cm, a mean value of 10 cm, and a fat tail for positive anomalies at La Réole, Langon and Pessac. Upstream of La Réole, Langon and Pessac, the PDF is symmetric on the Garonne and Dordogne rivers with a standard deviation of about 1.8 m for the flood rise and storm peak, leading to anomalies up to 1 m and a standard deviation of about 0.6 m for ebb tide and low flow. Along the estuary and in the maritime area, the PDF is rather symmetric. The standard deviation decreases from the confluence at Bec d'Ambès to the mouth of the estuary. The standard deviation over the estuary, except in the fluvial area, is larger for flood tide and storm peak than for ebb tide and low flow. This behavior can be explained by the hypersynchronous shape of the estuary which amplifies perturbations from the maritime boundary conditions along the estuary at flood tide. Moreover, it reflects respectively the predominance of the gaussian perturbation of the maritime signal and the uniform perturbation of the Strickler coefficient with a non-linear behavior in the fluvial part.

3.3 Global sensitivity analysis indices for aggregated modes

3.3.1 Temporal analysis

Sobol' indices are displayed with a blue-red color bar for the 8 uncertain inputs X_i (Sect. 2.3.1) in Fig. 9, along the curvilinear abscissa (x-axis) and over time (y-axis). The total Sobol' indices are plotted for each input variable. Blue/red means small/large Sobol' indices for X_i.
For the 2003 event studied here, Fig. 9 clearly shows the predominance of the maritime boundary conditions and the dependency of all variables on the tidal signal. The wind drag coefficient, the hydrological boundary conditions and the friction coefficient in area A_4 have no influence on the water level variability except at the upstream location of the Garonne and Dordogne rivers. Over the maritime area A_1, the water level variance is explained by the variance in the maritime boundary condition with Sobol' indices close to 1 from Royan (station 1) to Richard (station 5) near the mouth of the estuary. It should be noted that the fraction of the water level variance that is not explained by CLMAR is explained by Ks1. In estuarian area A_2, CLMAR and Ks2 are the most significant sources of uncertainty, with a large predominance of CLMAR at high tide. At low tide, the Sobol' index for Ks2 reaches 0.8. The influence of the maritime boundary condition decreases from Fort-Médoc (in A_2) to the confluence at Bec d'Ambès (in A_3) and the influence of Ks2 and Ks3 increases. For this event, in area A_4, the influences of CLMAR and Ks4 are alternatively predominant in coherence with the tidal signal. At La Réole and Pessac, Sobol' index for Ks4 reaches 0.8. It should be noted that the difference between total and first order indices, representing interactions of X_i with other uncertain variables, has been computed for all uncertain variables. As it is nearly equal to 0, it can be concluded that, for the 2003 storm, no interactions are detected between any input variable X_i. Total Sobol' indices and ranks are time-averaged and plotted in Fig. 10 along the curvilinear abscissa (x-axis) and for all X_i (y-axis). As expected, for the 2003 event, the maritime boundary conditions have a predominant impact along the entire domain, with the significant influence of friction coefficients, while hydrological boundary conditions have a limited impact to the upstream locations of the Garonne and Dordogne rivers.

3.3.2 Global sensitivity analysis space mapping

Figs 11-a (resp. -c) and 11-b (resp. -d) display maps of total Sobol' indices over the entire mesh of the variable

X_8 = CLMAR (resp. X_1 = Ks1), at the storm peak and at low tide respectively, for the 2003 event. These maps show the homogeneity of the total Sobol' indices geographical repartition and confirm that the conclusions drawn previously for the 26 locations of interest can be generalized for all points located in A_1, A_2, A_3 and A_4. The same maps have been obtained for all uncertain variables for the storm peak, ebb tide, low tide and flood tide, but are not shown here. As formerly observed, for the 2003 event, the wind drag coefficient (Cd), Dordogne river discharge (QDOR) and Garonne river discharge (QGAR) have a very small influence over the tidal cycle along the estuary. As 2003 event is a flood event for both rivers, further investigation is needed to confirm this conclusion. The uncertainty in the maritime boundary condition is predominant, especially during the flood tide and storm peak (at Royan) (Fig 11-a) along the estuary except at the upstream part of the Garonne and Dordogne rivers (in A_4), where friction coefficient Ks3 is the most dominant uncertain variable. Ks1 (displayed in panels c- and d-), Ks2 and Ks4 show no influence during the storm peak. During ebb tide, the influence of CLMAR propagates along the Garonne and Dordogne rivers, while the upstream parts of the rivers remain fully under the influence of Ks3. At low tide, Fig. 11-b shows that the influence of CLMAR returns to the middle part of the estuary in A_2, whereas Ks1 (resp. Ks2) is the most dominant uncertain variable farther downstream (resp. upstream), consistent with the tidal signal. The influence of Ks3 in the upstream part of the Dordogne and Garonne rivers propagates to A_4. The Gironde Estuary hydrodynamics are the result of interplays between time and/or space dependent processes, such as friction, convergence of the estuary and maritime and fluvial usptream boundary conditions, but also of the memory of the state of the system. UQ and GSA help to identify and understand the evolution of complex physical processes that drive the Gironde estuary and are not entirely intuitive, in particular, when considering their phase with the tidal cycle.

3.4 Focus on the eigenmodes of the maritime boundary forcings

A GSA study dedicated to the maritime boundary forcing was performed considering each eigenmode of the KL decomposition for the 7-day 2003 event. The other parameters (Ks1, Ks2, Ks3, Ks4, QGAR and QDOR) are not perturbed and their associated values are their mean values. Table 4 shows the variance associated with each orthogonal function of the KL decomposition of the Gaussian correlation function with its time scale set to 6 hours (half-tide). No clear predominance of the first modes is observed with about 6 % of the input variance explained by the first 4 modes and 1 % for the following 19 modes. The accumulated variance explained by the first 7 modes kept for the GSA is about 45 %. The Sobol' indices associated with these modes are plotted in Fig. 12. Their contributions are linked to the tide cycle but are asynchronous. The influence of the eigenmodes decreases from the mouth of the estuary to the upstream part of the rivers with respect to the periodic tide signal. Modes 2, 3, 4 and 5 have major contributions, their respective Sobol' indices reaching 30 %, whereas modes 6 and 7 have less influence during the second part of the storm event and mode 1 has no influence on water levels except at the end of the event when its total Sobol' index reaches 20 %. The uncertainty in the tide and surge level was estimated by [43] to be respectively 5 cm and 40 cm for a 36-hour lead time. This suggests dividing the maritime signal uncertainty into a deterministic tidal contribution and a stochastic surge level contribution caused by the meteorological forcings [44] as well as the tide/surge level interactions [45] through surge levels. Further work should thus focus on separating the tidal signal from the surge level signal. The correlation time scale calculated from the surge level time series provided by Meteo-France is about 2.1 days. Only 14 eigenmodes (resp. 4) are required to represent 99 % (resp. 90 %) of the total variance of the signal, as shown in Fig. 13.

4 Conclusions and perspectives

The Telemac2D numerical model used for operational flood forecasting by FFS GAD in the Gironde estuary was used for a GSA based on ANOVA to estimate the Sobol' indices over a 7-day storm event in 2003. It was shown that the maritime boundary conditions drive the dynamics of the estuary.

Moving from the mouth of the estuary to the upstream part of the Garonne and Dordogne rivers, the influence of the friction coefficient increases, and the hydrological forcing has a very local influence upstream in the rivers. This GSA study allows the identification of the most significant sources of uncertainty. Once identified, these uncertainties should be reduced, for instance with a data assimilation algorithm such as Ensemble Kalman Filter, in order to improve the water level in the estuary in simulation and forecast mode. A perspective for this study is to take into account uncertainties in the surface forcing atmospheric fields (wind and pressure). Further work should also focus on the formulation of a surrogate model for the 2D Gironde hydraulics model

for high flow discharges in order to reduce the cost of the GSA and the ensemble assimilation. Gaussian Process or Polynomial Chaos surrogates have been used for UQ and GSA in the context of hydraulics ([46], [23]). Both methods proved efficient for metamodelling of the SWE with the 1D solver Mascaret ([47], [48]) for GSA with Sobol' indices and covariance matrix estimation. A polynomial surrogate was also implemented for Telemac2D on the Garonne river and allowed for a cost-reduced computation of the sensitivity indices [23]. This work should be extended to the Gironde estuary taking into account scalar and field uncertainties. The proposed surrogate modeling and data assimilation approaches would meet this need and would result in a reduced-cost ensemble based data assimilation algorithm to reduce major sources of uncertainties and improve water level forecasting in the Gironde estuary.

A Appendix A

Sobol' indices [35] measure the contributions of the different independent inputs $X_1, X_2, \ldots, X_d$ and their interactions in the variance V(Y) of the output $Y = f(X)$ with $X = (X_1, X_2, \ldots, X_d)$, $E((f(X))^2) < \infty$ and f the model. They are based on the Hoeffding decomposition of f [49],

$$\begin{aligned} f(X) =& f_\emptyset + \sum_{i \subseteq I_d} f_i(X_i) \\ &+ \sum_{\substack{\{i,j\} \subseteq I_d^2 \\ j>i}} f_{i,j}(X_i, X_j) \\ &+ \ldots + f_{1,2,\ldots,d}(X_1, X_2, \ldots, X_d) \\ &= \sum_{u \subseteq I_d} f_u(X_u) \end{aligned} \tag{12}$$

where $I_d = \{1, \ldots, d\}$ is the set of input indices, $f_\emptyset = E(Y)$ is the expectation of Y (here the average of all values Y can take), $f_i(X_i) = E(Y|X_i) - f_\emptyset$ is the elementary contribution of X_i to $f(X)$, and $f_{i,j}(X_i, X_j) = E(Y|X_i, X_j) - f_i(X_i) - f_j(X_j) - f_\emptyset$ is the contribution of the interaction between X_i and X_j to $f(X)$.

From Eq. (12) and using the orthogonality condition $E(f_i f_j) = 0$ if $i \neq j$, the variance of Y is:

$$V(Y) = \sum_{i \subseteq I_d} V_i + \sum_{\substack{\{i,j\} \subseteq I_d^2 \\ j>i}} V_{i,j} + \ldots + V_{1,2,\ldots,d} = \sum_{u \subseteq I_d} V_u \tag{13}$$

where $V_i = V(f_i(X_i))$ is the elementary contribution of X_i to $V(Y)$, $V_{i,j} = V(f_{i,j}(X_i, X_j))$ is the contribution of the interaction between X_i and X_j to $V(Y)$, and so on. Dividing Eq. (13) by $V(Y)$ leads to Eq. (8).

B Appendix B

This appendix describes the main steps for the stochastic estimation of the Sobol' indices of the different independent inputs $X_1, X_2, \ldots, X_d$ with $X = (X_1, X_2, \ldots, X_d)$ according to [10].

1. Step 1: generation of two ensembles of size N_e for the normalized input parameters set $(x_1, x_2, \ldots, x_d)$. The first (resp. second) (N_e, d) matrix is denoted by A (resp. B) (Eq. (14) (resp. (Eq. (15)))). The space filling strategy is carried out with a Sobol' sequence rather than a classical Monte-Carlo strategy:

$$A = \begin{pmatrix} x_1^{(1)} & x_2^{(1)} & \cdots & x_i^{(1)} & \cdots & x_d^{(1)} \\ x_1^{(2)} & x_2^{(2)} & \cdots & x_i^{(2)} & \cdots & x_d^{(2)} \\ \cdots & \cdots & \cdots & \cdots & \cdots & \cdots \\ x_1^{(Ne-1)} & x_2^{(Ne-1)} & \cdots & x_i^{(Ne-1)} & \cdots & x_d^{(Ne-1)} \\ x_1^{(Ne)} & x_2^{(Ne)} & \cdots & x_i^{(Ne)} & \cdots & x_d^{(Ne)} \end{pmatrix} \tag{14}$$

$$B = \begin{pmatrix} x_1^{(Ne+1)} & x_2^{(Ne+1)} & \cdots & x_i^{(Ne+1)} & \cdots & x_d^{(Ne+1)} \\ x_1^{(Ne+2)} & x_2^{(Ne+2)} & \cdots & x_i^{(Ne+2)} & \cdots & x_d^{(Ne+2)} \\ \cdots & \cdots & \cdots & \cdots & \cdots & \cdots \\ x_1^{(2Ne-1)} & x_2^{(2Ne-1)} & \cdots & x_i^{(2Ne-1)} & \cdots & x_d^{(2Ne-1)} \\ x_1^{(2Ne)} & x_2^{(2Ne)} & \cdots & x_i^{(2Ne)} & \cdots & x_d^{(2Ne)} \end{pmatrix} \tag{15}$$

2. Step 2: definition of d matrices C_i formed by all columns of A except the i^{th} column taken from B [49].

3. Step 3: computation of the model output (and QoI) y_A (resp. y_B and y_{C_i} with $i = 1, , d$), for all the input values in the sample matrix A (resp. B and the d matrices C_i), obtaining $(d+2)$ vector outputs of dimension N_e: $y_A = f(A)$, $y_B = f(B)$, $y_{C_i} = f(C_i)$ with $i = 1, , d$.

[49], [50] and [51] describe the best approach to compute simultaneously S_i and S_{T_i} for each input variable.
In this study, the following estimators have been chosen for:
$V_{X_i}(E_{X_i}(Y|X_i)) = \frac{1}{N}\sum_{j=1}^{N} y_B^{(j)}\left(y_{C_i}^{(j)} - y_A^{(j)}\right)$,
$E_{X_i}(V_{X_i}(Y|X_i)) = \frac{1}{2N}\sum_{j=1}^{N}\left(y_A^{(j)} - y_{C_i}^{(j)}\right)^2$ and
$V(Y) = \frac{1}{N}\sum_{j=1}^{N}\left(y_A^j\right)^2 - f_0^2$
with $f_0^2 = \frac{1}{N}\sum_{j=1}^{N} y_A^j y_B^j$.
Anomalies due to an uncertain variable X_i corresponding to the normalized uncertain variable x_i are defined as $y_{C_i} - y_A$ and represent the part of the QoIs output resulting from X_i only.
If $(X_i)_{i=k,,k+m}$ correspond to the m uncertain modes of a field input, the contribution of each mode can be estimated separately with the methodology described above. The whole contribution of the field input can also be estimated by processing the uncertain variable modes in one block and by defining a matrix C_k formed by all columns of A except the k^{th} to $(k+m)^{\text{th}}$ columns taken from B.

C Appendix C

A truncated form $q_p(t)$ (resp. $h_p(t)$) of $q(t)$ (resp. $h(t)$) is formulated with a KL decomposition [20] of $q(t)$ (resp. $h(t)$):

$$q_p(t) = \sum_{i=1}^{p} \sqrt{\lambda_i}\phi_i(t)\,\epsilon_i \tag{16}$$

where ϵ_i are independent standard Gaussian variables and (λ_i, ϕ_i) are the i^{th} eigenvalue and eigenfunction of κ, the solution of the Fredholm equation [39]:

$$\int \kappa(t,\tau)\,\phi_i(\tau)\,d\tau = \lambda_i \phi_i(t) \tag{17}$$

with $\int \phi_i(t)\phi_j(t)dt = \delta_{i,j}$.

References

1. Jaak Monbaliu, Zhongyuan Chen, Didier Felts, Jianzhong Ge, Francois Hissel, Jens Kappenberg, Siddharth Narayan, Robert J Nicholls, Nino Ohle, Dagmar Schuster, et al. Risk assessment of estuaries under climate change: lessons from western europe. Coastal Engineering, 87:32–49, 2014.
2. Maryam Golnaraghi. Institutional partnerships in multi-hazard early warning systems: a compilation of seven national good practices and guiding principles. Springer Science & Business Media, 2012.
3. Jean-Michel Hervouet. Hydrodynamics of free surface flows: modelling with the finite element method. John Wiley & Sons, 2007.
4. François Hissel. Projet gironde – rapport final d'évaluation du modèle gironde. Technical report, CETMEF, 2010.
5. AH Weerts, HC Winsemius, and JS Verkade. Estimation of predictive hydrological uncertainty using quantile regression: examples from the national flood forecasting system (england and wales). Hydrology and Earth System Sciences, 15(1):255–265, 2011.
6. Bertrand Iooss and Paul Lemaître. A review on global sensitivity analysis methods. In Uncertainty management in simulation-optimization of complex systems, pages 101–122. Springer, 2015.
7. Bradley Efron. Linear statistical inference and its applications., 1967.
8. Bradley Efron and Charles Stein. The jackknife estimate of variance. The Annals of Statistics, pages 586–596, 1981.
9. Toshimitsu Homma and Andrea Saltelli. Importance measures in global sensitivity analysis of nonlinear models. Reliability Engineering & System Safety, 52(1):1–17, 1996.
10. William Becker and Andrea Saltelli. Design for sensitivity analysis. In Handbook of design and analysis of experiments, pages 647–694. Chapman and Hall/CRC, 2015.
11. Chonggang Xu and George Zdzislaw Gertner. Uncertainty and sensitivity analysis for models with correlated parameters. Reliability Engineering & System Safety, 93(10):1563–1573, 2008.
12. Jia Li and Dongbin Xiu. On numerical properties of the ensemble kalman filter for data assimilation. Computer Methods in Applied Mechanics and Engineering, 197(43-44):3574–3583, 2008.
13. Bertrand Iooss and Andrea Saltelli. Introduction to sensitivity analysis. Handbook of uncertainty quantification, pages 1103–1122, 2017.
14. Bertrand Iooss, Loïc Boussouf, Vincent Feuillard, and Amandine Marrel. Numerical studies of the metamodel fitting and validation processes. arXiv preprint arXiv:1001.1049, 2010.
15. Matieyendou Lamboni, Hervé Monod, and David Makowski. Multivariate sensitivity analysis to measure global contribution of input factors in dynamic models. Reliability Engineering & System Safety, 96(4):450–459, 2011.
16. Olivier Le Maître and Omar M Knio. Spectral methods for uncertainty quantification: with applications to computational fluid dynamics. Springer Science & Business Media, 2010.
17. Andrea Saltelli and Michaela Saisana. Settings and methods for global sensitivity analysis–a short guide. In PAMM: Proceedings in Applied Mathematics and Mechanics, volume 7, pages 2140013–2140014. Wiley Online Library, 2007.
18. Géraud Blatman. Adaptive sparse polynomial chaos expansions for uncertainty propagation and sensitivity analysis. PhD thesis, Clermont-Ferrand 2, 2009.
19. C Audouze, F De Vuyst, and PB Nair. Reduced-order modeling of parameterized pdes using time–space-parameter principal component analysis. International journal for numerical methods in engineering, 80(8):1025–1057, 2009.
20. Gal Berkooz, Philip Holmes, and John L Lumley. The proper orthogonal decomposition in the analysis of turbulent flows. Annual review of fluid mechanics, 25(1):539–575, 1993.
21. Charlotte M Emery, Sylvain Biancamaria, Aaron Boone, Pierre-André Garambois, Sophie Ricci, Mélanie C Rochoux, and Bertrand Decharme. Temporal variance-based sensitivity analysis of the river-routing component of the large-scale hydrological model isba–trip: Application on the amazon basin. Journal of Hydrometeorology, 17(12):3007–3027, 2016.
22. Jiri Nossent, Pieter Elsen, and Willy Bauwens. Sobol' sensitivity analysis of a complex environmental model. Environmental Modelling & Software, 26(12):1515–1525, 2011.
23. Nicole Goutal, Cedric Goeury, Riadh Ata, Sophie Ricci, Nabil El Mocayd, M Rochoux, Hind Oubanas, Igor Gejadze, and Pierre-Olivier Malaterre. Uncertainty quantification for river flow simulation applied to a real test case: The garonne valley. In Advances in Hydroinformatics, pages 169–187. Springer, 2018.
24. Hind Oubanas, Igor Gejadze, Pierre-Olivier Malaterre, and Franck Mercier. River discharge estimation from synthetic swot-type observations using variational data assimilation and the full saint-venant hydraulic model. Journal of Hydrology, 559:638–647, 2018.
25. Amandine Marrel, Nathalie Saint-Geours, and Matthias De Lozzo. Sensitivity analysis of spatial and/or temporal phenomena. Handbook of Uncertainty Quantification, pages 1–31, 2016.
26. Katrin Erdlenbruch, Éric Gilbert, Frédéric Grelot, and Chritophe Lescoulier. Une analyse coût-bénéfice spatialisée de la protection contre des inondations. application de la méthode des dommages évités à la basse vallée de l'orb. Ingénieries-EAT, (53):p–3, 2008.
27. Guotu Li, Mohamed Iskandarani, Matthieu Le Hénaff, Justin Winokur, Olivier P Le Maître, and Omar M Knio. Quantifying initial and wind forcing uncertainties in the gulf of mexico. Computational Geosciences, 20(5):1133–1153, 2016.
28. Patrice Castaing and George P Allen. Mechanisms controlling seaward escape of suspended sediment from the gironde: a macrotidal estuary in france. Marine Geology, 40(1-2):101–118, 1981.
29. Nicolas Huybrechts, Catherine Villaret, and Florent Lyard. Optimized predictive two-dimensional hydrodynamic model of the gironde estuary in france. Journal of Waterway, Port, Coastal and Ocean Engineering, 138(4):312–322, 2011.
30. François Hissel, Gilles Morel, Gianluca Pescaroli, Herman Graaff, Didier Felts, and Luca Pietrantoni. Early warning

and mass evacuation in coastal cities. Coastal Engineering, 87:193–204, 2014.
31. Ph Gauckler. Etudes Théoriques et Pratiques sur l'Ecoulement et le Mouvement des Eaux. Gauthier-Villars, 1867.
32. M Janišková. Study of the systematic errors in aladin associated to the physical part of the model. Note Aladin, (7), 1995.
33. Florence Levy. Construction d'un modéle de surcotes sur la façade atlantique. Technical report, CETMEF, 2013. rapport provisoire.
34. Florence Levy and Antoine Joly. Modélisation des surcotes avec telemac2d. Technical report, EDF/LHSV, 2013. rapport EDF à accessibilité restreinte.
35. Andrea Saltelli and Il'ya Meerovich Sobol'. Sensitivity analysis for nonlinear mathematical models: numerical experience. Matematicheskoe Modelirovanie, 7(11):16–28, 1995.
36. Roger A Flather. Results from a storm surge prediction model of the north-west european continental shelf for april, november and december, 1973. 1976.
37. Jin Wu. Wind-stress coefficients over sea surface near neutral conditions—a revisit. Journal of Physical Oceanography, 10(5):727–740, 1980.
38. Margaret Yelland and Peter K Taylor. Wind stress measurements from the open ocean. Journal of Physical Oceanography, 26(4):541–558, 1996.
39. Siegfried Prössdorf and Bernd Silbermann. Numerical analysis for integral and related operator equations. Operator theory, 52:5–534, 1991.
40. Allan H Murphy. A new vector partition of the probability score. Journal of Applied Meteorology, 12(4):595–600, 1973.
41. O Talagrand, R Vautard, and B Strauss. Evaluation of probabilistic prediction systems, paper presented at ecmwf workshop on predictability, eur. cent. for med. range weather forecasts. Reading, UK, 1997.
42. Guillem Candille and Olivier Talagrand. Evaluation of probabilistic prediction systems for a scalar variable. Quarterly Journal of the Royal Meteorological Society, 131(609):2131–2150, 2005.
43. Loren Carrère, Florent Lyard, M Cancet, A Guillot, and Laurent Roblou. Fes 2012: a new global tidal model taking advantage of nearly 20 years of altimetry. In 20 Years of Progress in Radar Altimatry, volume 710, 2013.
44. Riccardo Mel, Daniele Pietro Viero, Luca Carniello, Andrea Defina, and Luigi D'Alpaos. Simplified methods for real-time prediction of storm surge uncertainty: The city of venice case study. Advances in water resources, 71:177–185, 2014.
45. D Idier, H Muller, R Pedreros, J Thiébot, M Yates, R Créach, G Voineson, F Dumas, F Lecornu, L Pineau-Guillou, et al. Système de prévision de surcotes en manche/atlantique et méditerranée: Amélioration du système existant sur la façade manche/gascogne [d4]. Technical report, Rapport BRGM/RP-61019-FR, 2012.
46. Amandine Marrel. Mise en oeuvre et utilisation du métamodèle processus gaussien pour l'analyse de sensibilité de modèles numériques: application à un code de transport hydrogéologique. PhD thesis, Toulouse, INSA, 2008.
47. Nabil El Moçayd. La décomposition en polynôme du chaos pour l'amélioration de l'assimilation de données ensembliste en hydraulique fluviale. PhD thesis, 2017.
48. Pamphile T Roy, Nabil El Moçayd, Sophie Ricci, Jean-Christophe Jouhaud, Nicole Goutal, Matthias De Lozzo, and Mélanie C Rochoux. Comparison of polynomial chaos and gaussian process surrogates for uncertainty quantification and correlation estimation of spatially distributed open-channel steady flows. Stochastic Environmental Research and Risk Assessment, 32(6):1723–1741, 2018.
49. Andrea Saltelli and Paola Annoni. How to avoid a perfunctory sensitivity analysis. Environmental Modelling & Software, 25(12):1508–1517, 2010.
50. Michiel JW Jansen. Analysis of variance designs for model output. Computer Physics Communications, 117(1-2):35–43, 1999.
51. Andrea Saltelli. Making best use of model evaluations to compute sensitivity indices. Computer physics communications, 145(2):280–297, 2002.

Table 1: Calibrated Strickler (K) coefficients computed from the $Nash_{HT}$ and $RMSE$ criteria.

Input variable	Updated Strickler coefficients with $Nash_{HT}$ criterion	Updated Strickler coefficients with $RMSE$ criterion	Range of uniform distribution
Ks1	55	70	[50 ; 70]
Ks2	70	70	[45 ; 75]
Ks3	75	65	[25 ; 75]
Ks4	50	55	[40 ; 80]
Cd	2.57.10-6	2.57.10-6	[0.678.10-6 ; 3.016.10-6]

Table 2: *Nash* at high tides ($Nash_{HT}$), $RMSE$ and $RMSE$ at high tides ($RMSE_{HT}$) for the 1999 and 2003 events along the Gironde estuary

Station	$Nash_{HT}$		$RMSE$ (m)		$RMSE_{HT}$ (m)	
	1999	2003	1999	2003	1999	2003
Verdon	-0.85	0.93	2.0	0.16	0.44	0.12
Richard	0.45	0.8	1.78	0.25	0.24	0.21
Laména	0.89	0.88	1.49	0.36	0.11	0.18
Pauillac	0.72	0.93	0.23	0.29	0.16	0.14
Fort Médoc	0.72	0.93	0.27	0.31	0.16	0.14
Bec d'Ambès	0.75	0.95	0.17	0.18	0.16	0.13
Le Marquis	0.53	0.95	0.28	0.24	0.22	0.12
Bassens	0.54	0.96	0.28	0.17	0.22	0.12
Bordeaux	0.59	0.96	0.23	0.18	0.21	0.13
La Réole			0.51	0.93		
Pessac			0.38	1.01		
Mean (without La Réole and Pessac)	0.48	0.92	0.75	0.24	0.21	0.15

Table 3: Computational costs for the 2003 event GSA.

Mesh (number of nodes)	Physical elapsed time (s)	Optimal nb. of cores for one run	Single run elapsed time (min)	Available nb. of cores for GSA	Ensemble size (Ne)	Total nb. of simulations for GSA (N)	GSA elapsed time (days)	Architecture
7351	250000	1	25	96	1000	25000	8	CentOS6 - Fedora 2 nodes 48 cores per node
7351	250000	1	25	96	5000	125000	40	CentOS6 - Fedora
418314	83400	112	13	2688	5000	125000	47	Intel Broadwell (2.4 GHz) 2 processors per node 14 cores per processor
418314	83400	32	1440	32768	7000	175000	71	BlueGene-Q 64 processors per node 16 cores per processor
418314	83400	32	1440	32768	10000	250000	101	BlueGene-Q 64 processors per node 16 cores per processor

Table 4: Eigenvalues and cumulated variances for the tide signal correlation function

mode rank	eigenvalue	cumulated variance	variance due to i	$\frac{(variance\ due\ to\ i)}{(variance\ due\ to\ the\ first\ mode}$
0	42829.68	6.69 %	6.69 %	1.0
1	41746.64	13.21 %	6.52 %	97.47 %
2	40054.17	19.46 %	6.26 %	93.52 %
3	37895.49	25.38 %	5.92 %	88.48 %
4	35429.63	30.92 %	5.53 %	82.72 %
5	32807.55	36.04 %	5.12 %	76.60 %
6	30156.19	40.75 %	4.71 %	70.41 %
7	27571.53	45.06 %	4.31 %	64.37 %
8	25118.82	48.98 %	3.92 %	58.65 %
9	22836.84	52.55 %	3.57 %	53.32 %
10	20743.96	55.79 %	3.24 %	48.43 %
11	18844.02	58.73 %	2.94 %	44.00 %
12	17131.37	61.40 %	2.68 %	40.00 %
13	15594.70	63.84 %	2.44 %	36.41 %
14	14219.79	66.06 %	2.22 %	33.20 %
15	12991.35	68.09 %	2.03 %	30.33 %
16	11894.18	69.95 %	1.86 %	27.77 %
17	10913.85	71.65 %	1.70 %	25.48 %
18	10037.04	73.22 %	1.57 %	23.43 %
19	9251.70	74.66 %	1.44 %	21.60 %
20	8547.08	76.00 %	1.33 %	19.96 %
21	7913.65	77.24 %	1.24 %	18.48 %
22	7343.06	78.38 %	1.15 %	17.14 %
23	6827.94	79.45 %	1.07 %	15.94 %

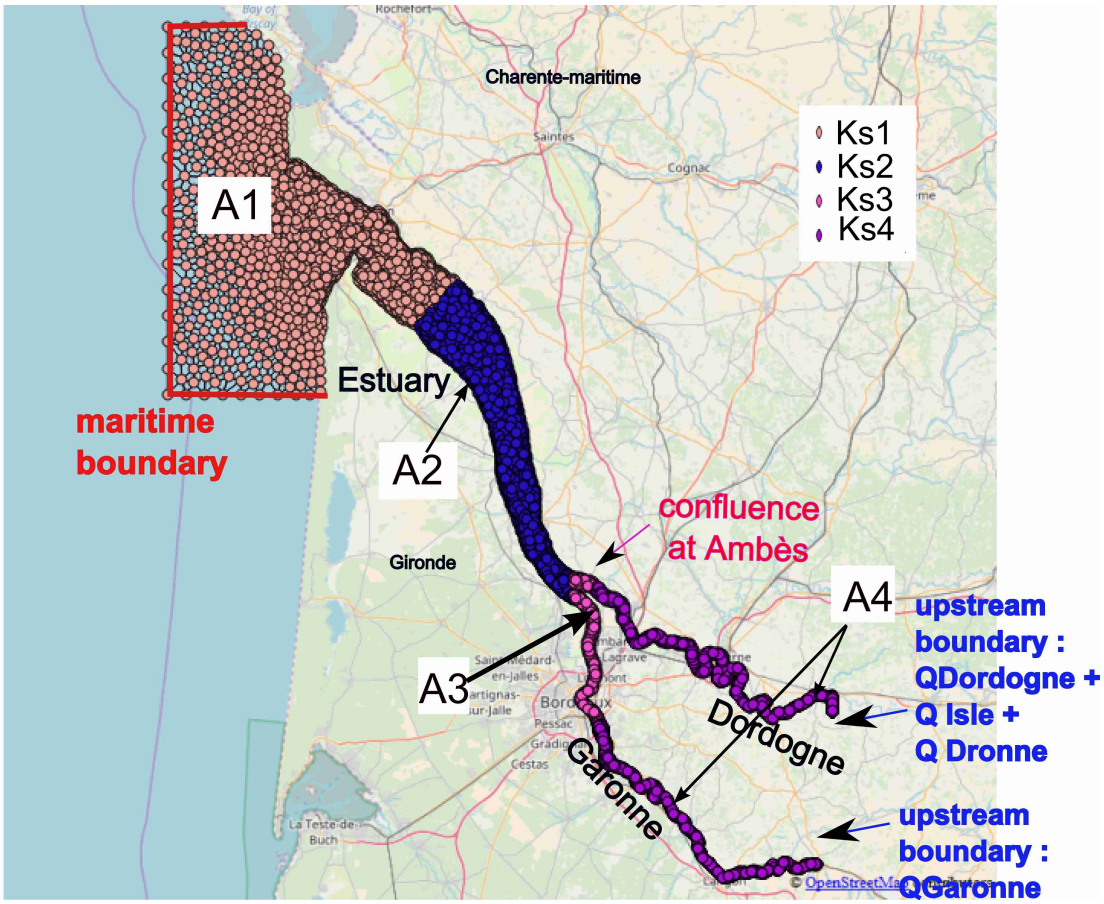

Fig. 1: Extension and location of the numerical model of the Gironde estuary and delimitation of the Strickler coefficient areas 1 to 4. Circles represent the nodes of the numerical model based on a mesh built with finite elements (in black).

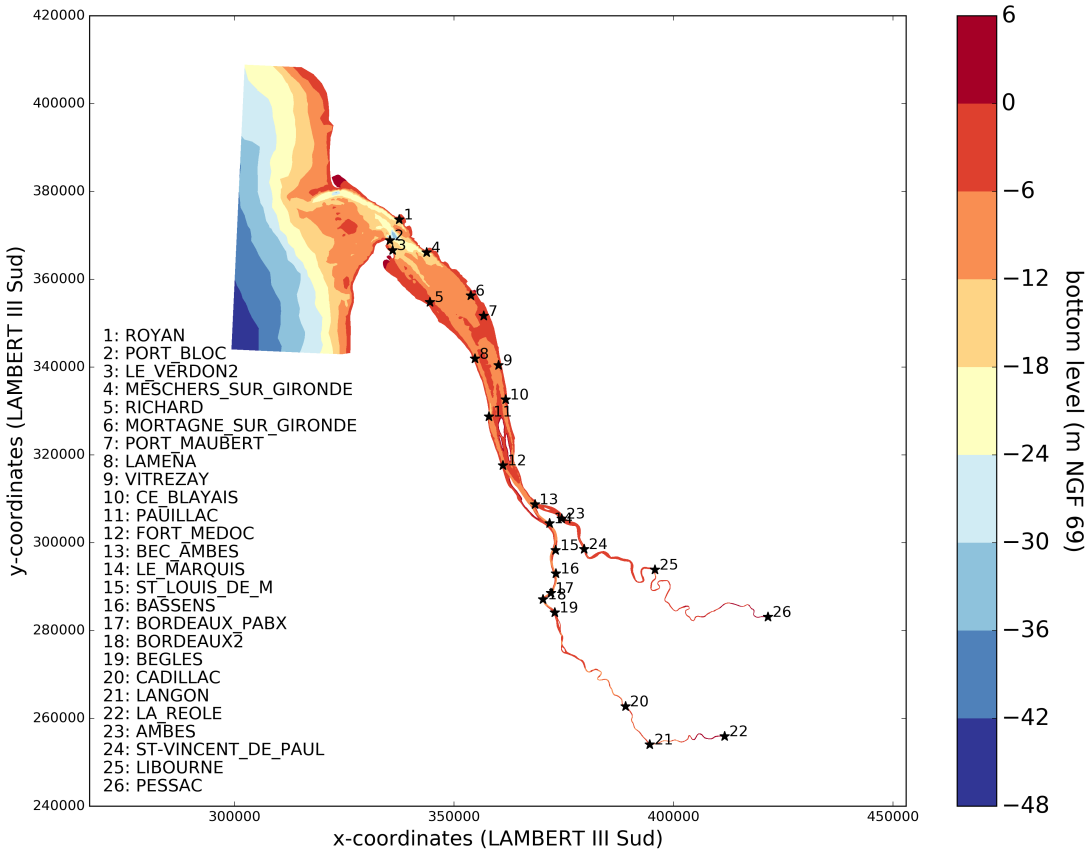

Fig. 2: Bathymetry (m NGF69) of the numerical model of the Gironde estuary. Stars show the 26 main stations of interest for the water level forecasts.

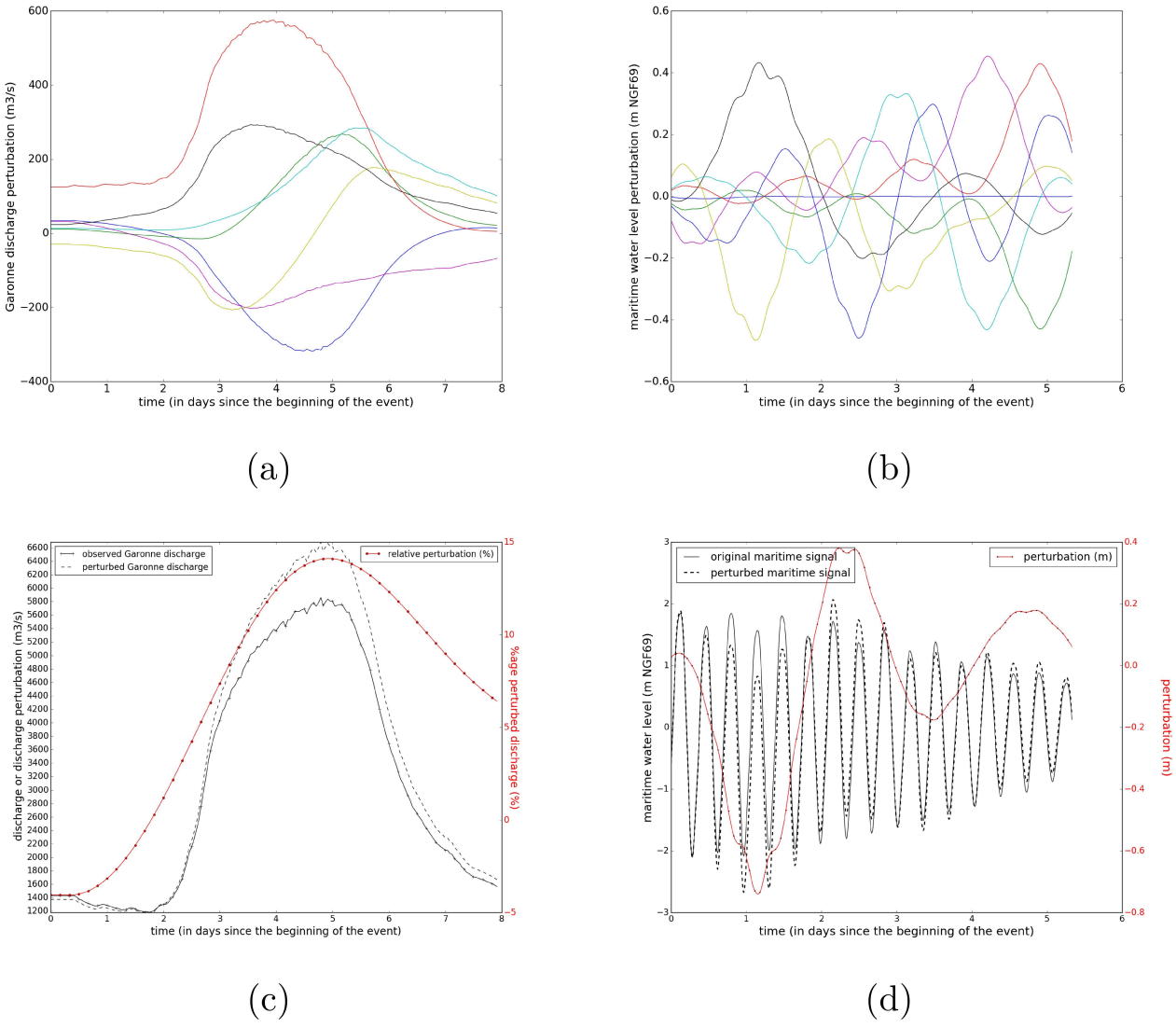

Fig. 3: Representation with time (since the beginning of the storm) during the February 2003 event of a sample of perturbations applied to the (a) Garonne river discharge and (b) maritime boundary conditions. Representation of (c) the reference Garonne river discharge (black line with crosses and left y-axis), of one perturbed member (black dotted line and left y-axis) and of the relative perturbation (red line marked with circles and right y-axis) and (d) the reference water level signal (black line and left y-axis) at one node of the maritime boundary, of one perturbed member (black dotted line and left y-axis) and of the perturbation (red line and right y-axis)

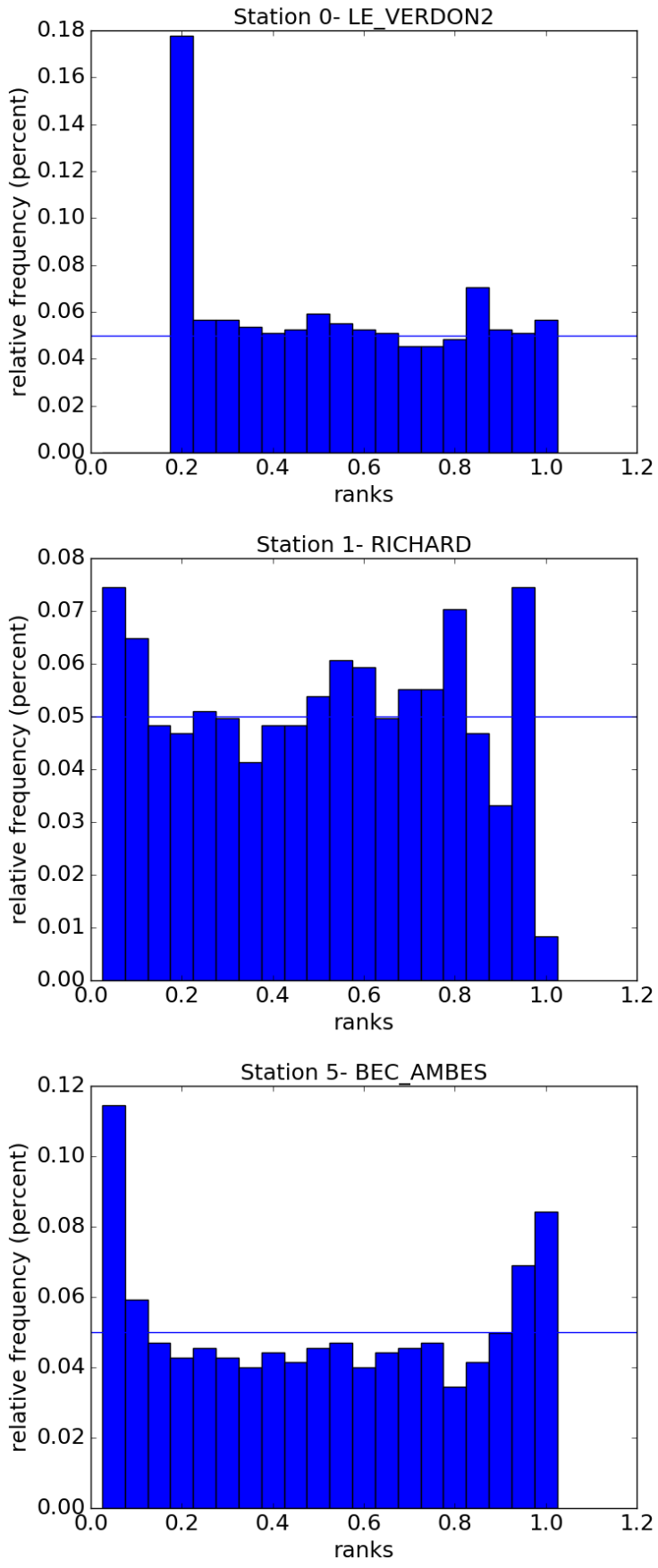

Fig. 4: Ranks diagrams for 3 stations along the Gironde estuary (Le Verdon at the mouth (top), Richard (middle) and Bec d'Ambès (bottom)).

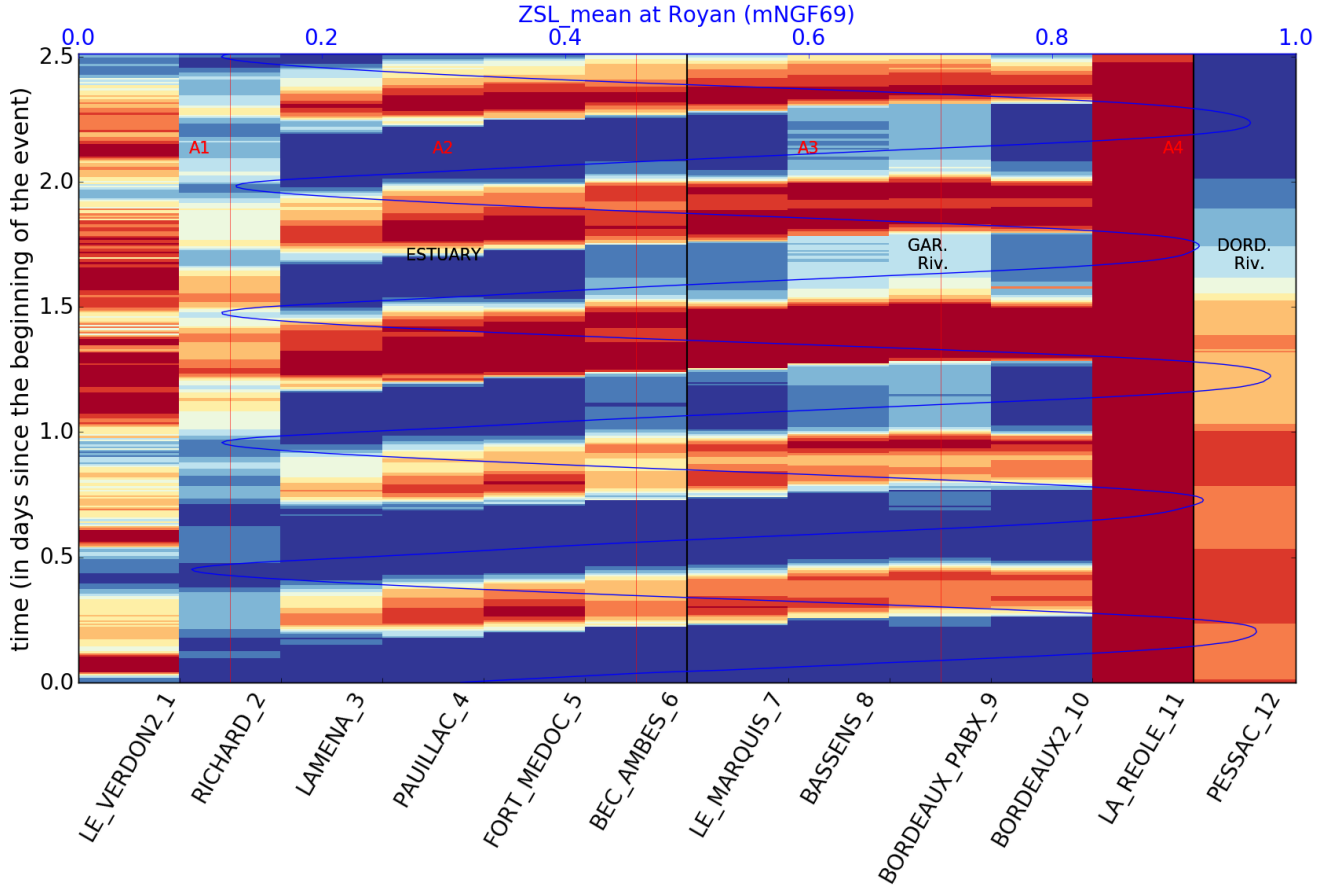

Fig. 5: Surface distribution of ranks along the Gironde estuary during the February 2003 storm. The black vertical lines represent the limits between the estuary, the confluence and the Garonne and Dordogne rivers. The x-axis displays the 12 observing stations classified from left to right from downstream to upstream, from Royan to the confluence at bec d'Ambès (1^{st} black vertical line), from the confluence to La Réole (Garonne river area located between both black vertical lines), and from the confluence to Pessac on the Dordogne river (Dordogne river area on the right of the 2^{nd} black vertical line). The red vertical lines represent the limits between the 4 friction coefficients areas (denoted by A_1, A_2, A_3 and A_4).

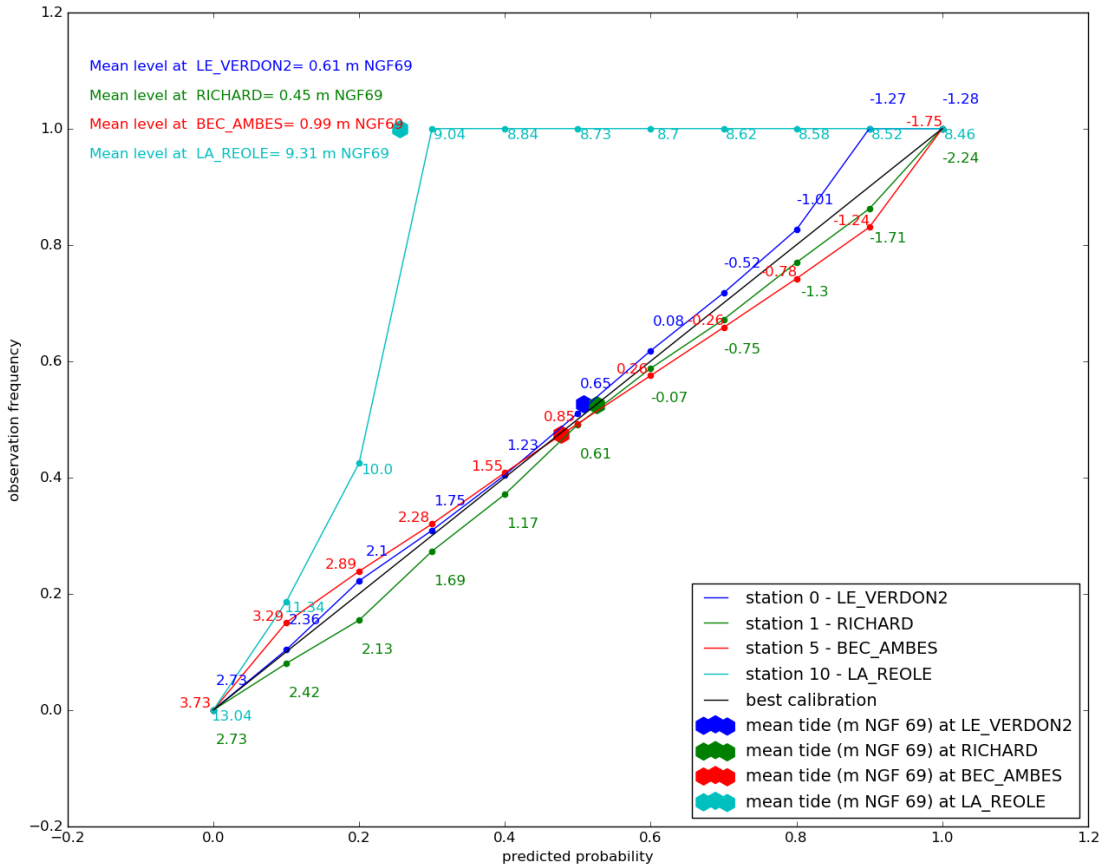

Fig. 6: Reliability diagram for 4 stations along the Gironde estuary (Le Verdon at the mouth (deep blue), Richard (green), Bec d'Ambès (red) and La Réole (cyan)) with corresponding observed water level quantiles during the 2003 event. Mean water levels at each station are represented with hexagons.

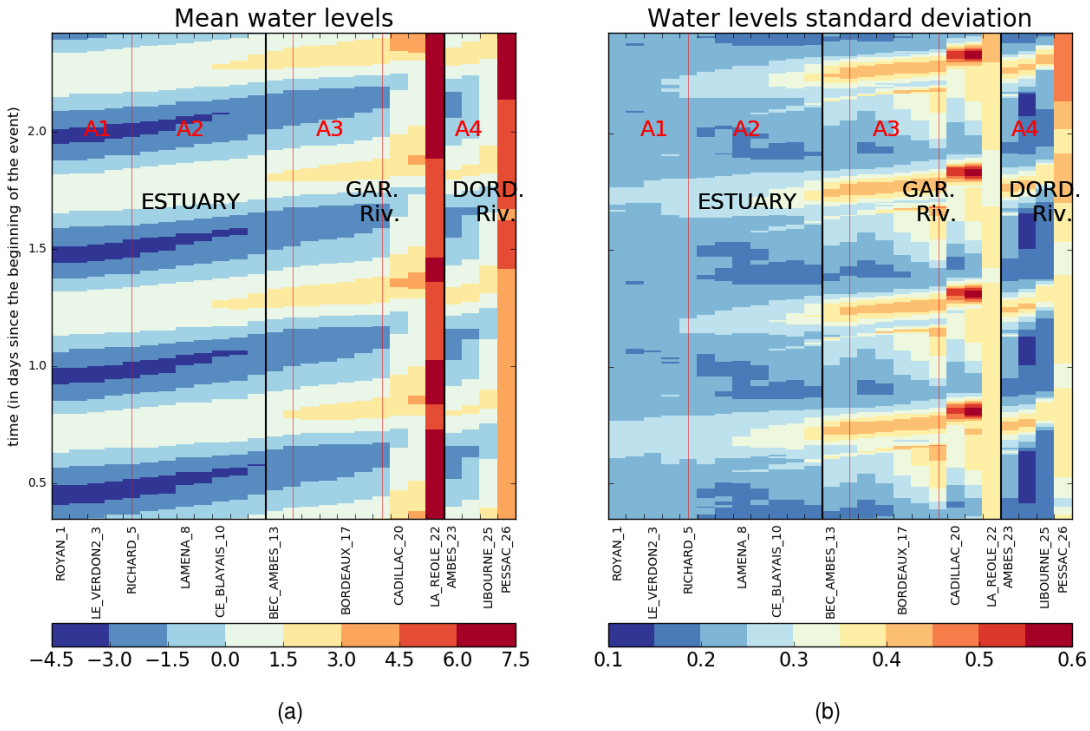

Fig. 7: Median (left) and standard deviation (right) of the water level outputs ensemble along the Gironde estuary during the February 2003 storm. The black vertical lines represent the limits between the estuary, the confluence and the Garonne and Dordogne rivers. The x-axis displays the 26 stations of interest classified from left to right for downstream to upstream, from Royan to the confluence at bec d'Ambès (1st black vertical line), from the confluence to La Réole (Garonne river area located between both black vertical lines) and from the confluence to Pessac on the Dordogne river (Dordogne river area on the right of the 2nd black vertical line). The red vertical lines represent the limits between the 4 friction coefficients areas (denoted by A_1, A_2, A_3 and A_4).

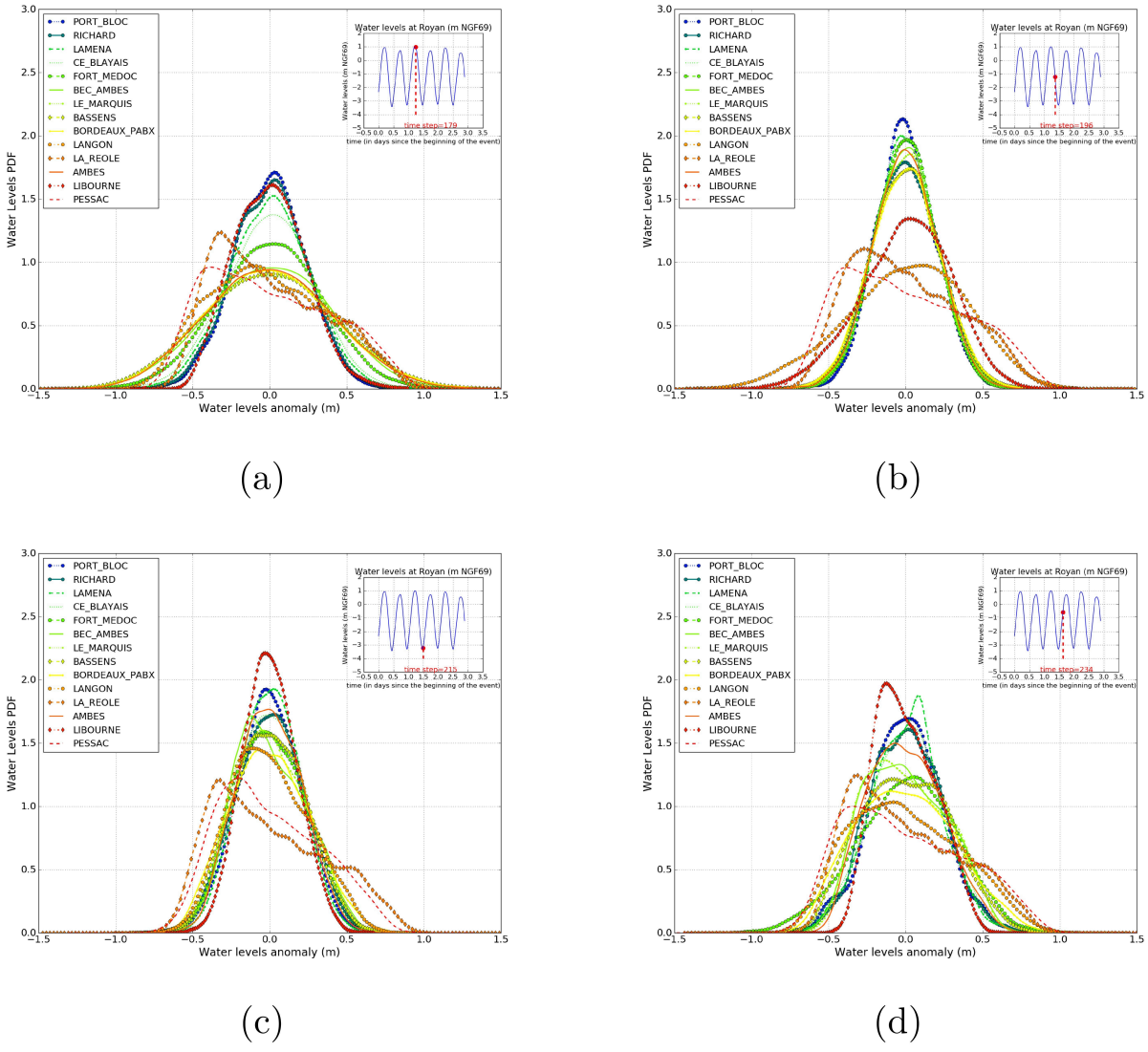

Fig. 8: Water level anomaly probability density functions along the Gironde estuary at the (a) storm peak, (b) ebb tide, (c) low tide, and (d) flood tide during the February 2003 storm.

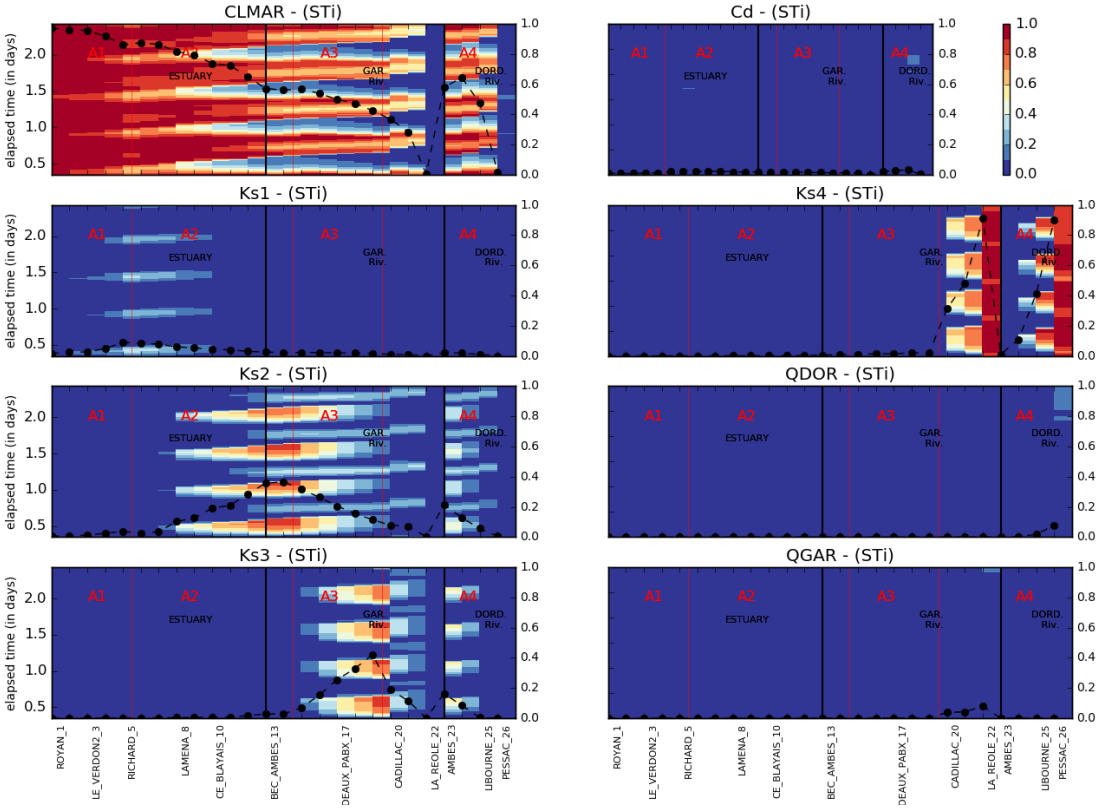

Fig. 9: Total Sobol' indices (STi) along the Gironde estuary during the February 2003 storm for 8 uncertain input variables (maritime boundary conditions (CLMAR), friction coefficients (Ks1, Ks2, Ks3, Ks4), the wind drag coefficient Cd and hydrological boundary conditions (Dordogne river discharge: QDOR; Garonne river discharge: QGAR). The x-axis is similar to that of Fig. 7, with the 26 stations of interest classified from left to right from downstream to upstream. The red vertical lines represent the limits between the 4 friction coefficient areas. The black vertical lines represent the limits between the estuary, the confluence, and the Garonne and Dordogne rivers. The thick dashed lines represent the time-averaged values for Sobol' indices along the Gironde estuary.

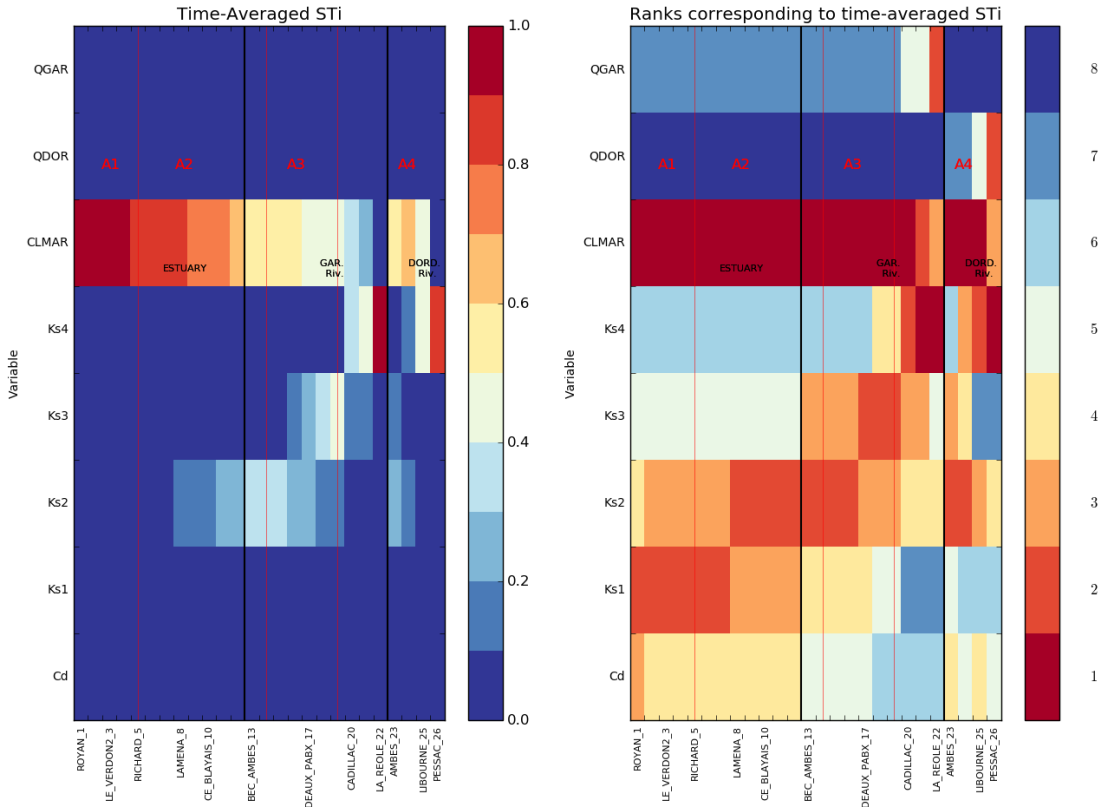

Fig. 10: representation of time averaged STi (left) and of the rank of the input variable with respect to STi (right) along the Gironde estuary during the February 2003 storm.

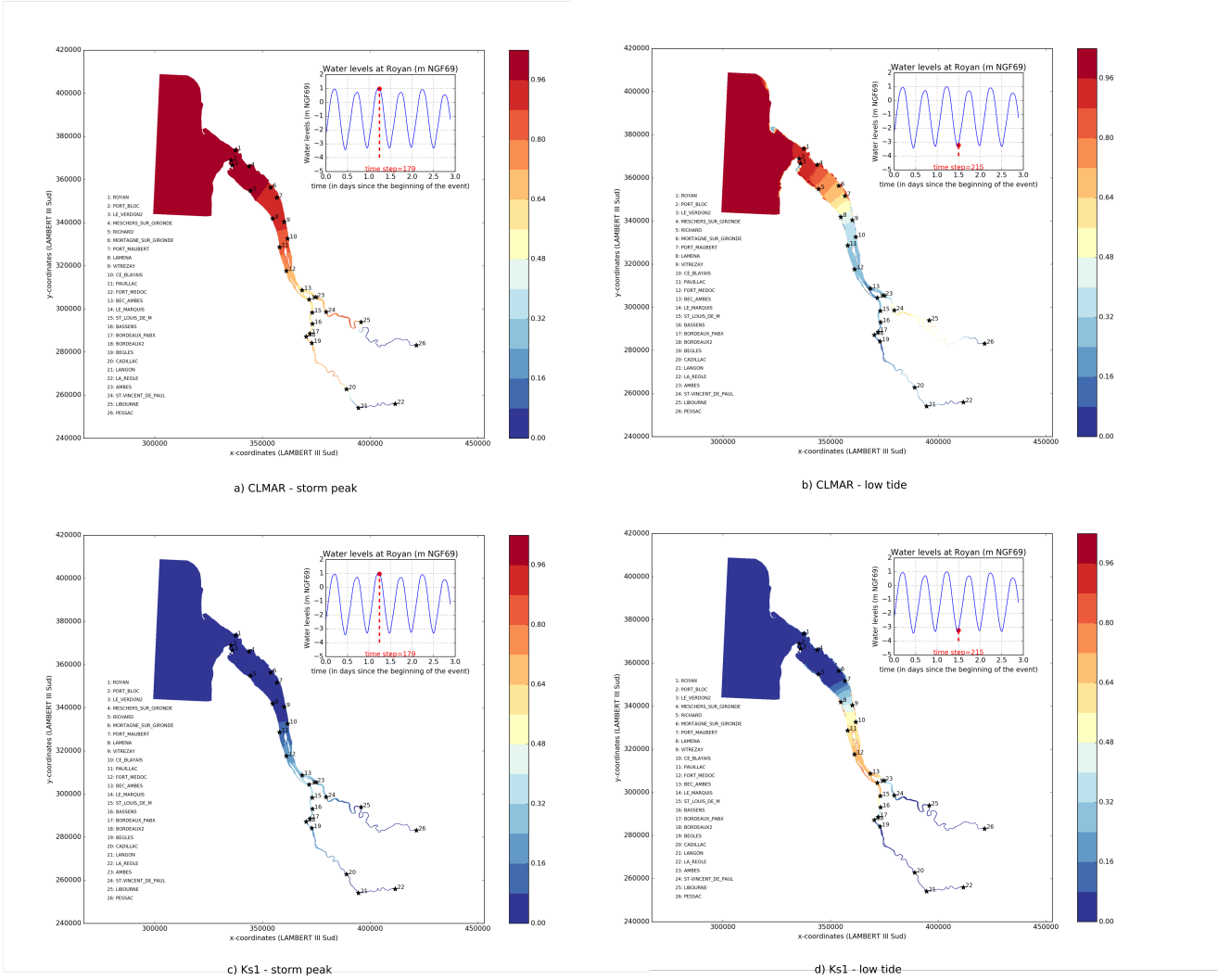

Fig. 11: Total Sobol' indices (STi) in the Gironde estuary at (a) (resp. (c)) storm peak and (b) (resp. (d)) low tide for uncertain variable maritime boundary condition CLMAR (resp. friction coefficient Ks1).

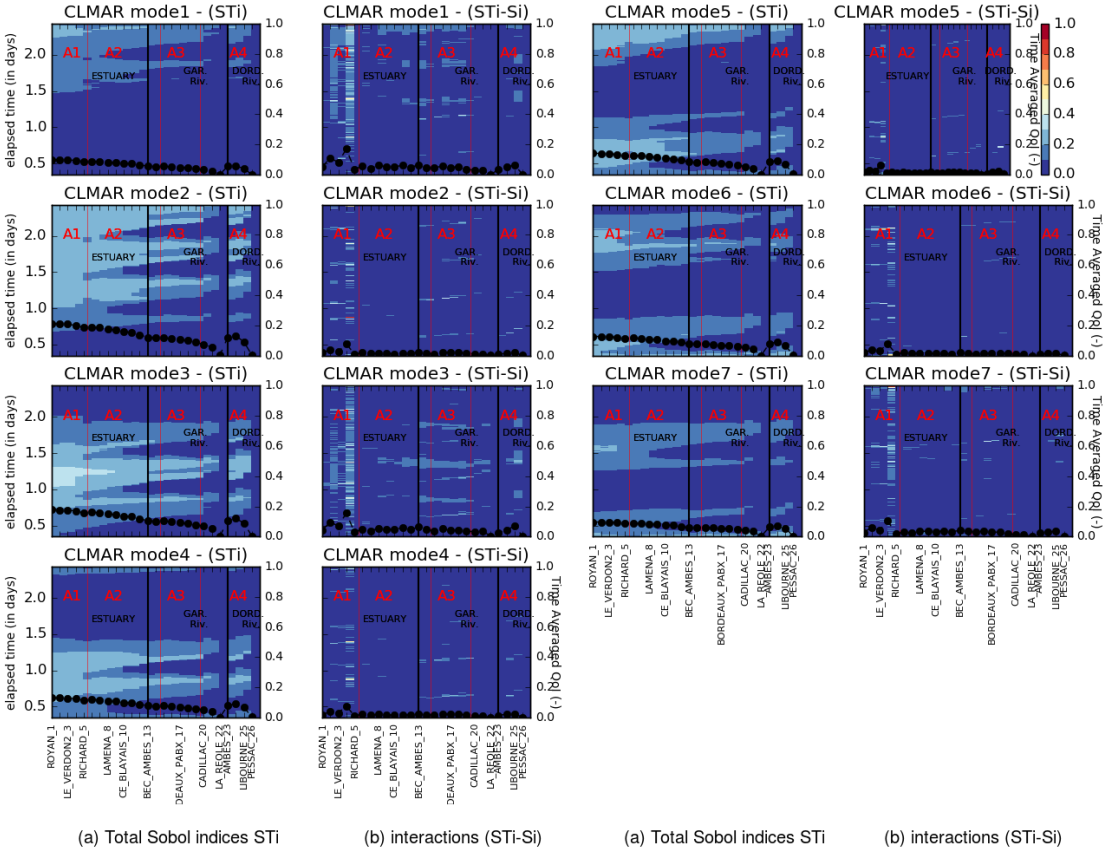

Fig. 12: Total Sobol' indices (STi) in panels a- (resp. interactions STi - Si in panels b-) along the Gironde estuary during the February 2003 storm for 7 uncertain input variables (maritime boundary (CLMAR) eigenmodes : mode1, mode2, mode3, mode4, mode5, mode6, mode7)

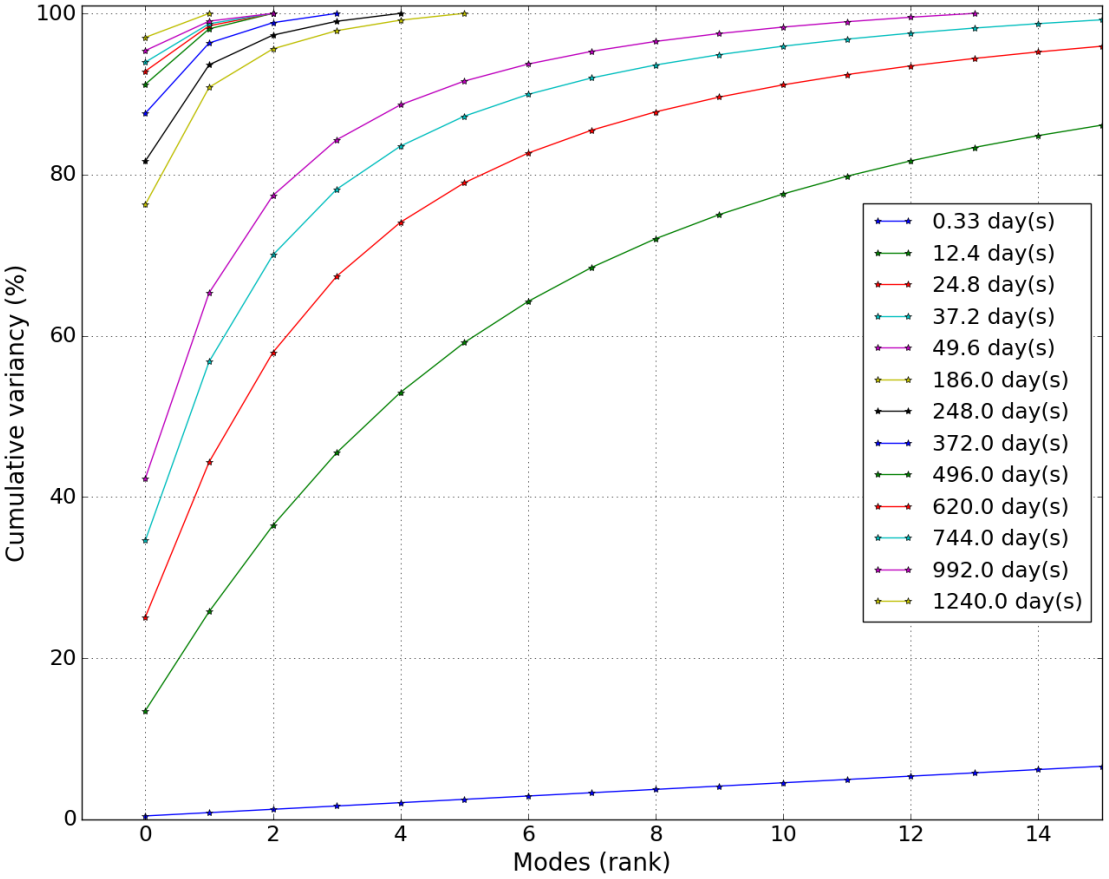

Fig. 13: Cumulated variance for the 14 first modes for several correlation time scales.